



Eidgenössische Technische Hochschule Zürich  
Swiss Federal Institute of Technology Zurich

# Characterization of Micromotion in a Linear Paul Trap & Optimization of a Two-Phase RF Drive

Master's Thesis

Björn Áki Jósteynsson  
bjosteins@ethz.ch

Trapped Ion Quantum Information Group  
Institute for Quantum Electronics  
Department of Physics, D-PHYS  
ETH Zürich

**Supervisors:**  
Nick Schwegler  
Dr. Daniel Kienzler  
Prof. Dr. Jonathan Home

April 14, 2023



I would like to thank the Molecule team for their tremendous support during this thesis. Firstly, David for the support in and out of the lab, giving advice on experiments and things to try out. Second, Daniel, for answering all my questions, taking the time to follow up on my ideas and for pointing me in the right directions when stuck. Lastly, I am especially grateful to Nick, for the supervision during the project, the invaluable assistance, discussions, brainstorming and encouragement. To Peter I express my sincere gratitude for the crucial help with the PCB, both during design and assembly.

To all members of the TIQI group, I thank you for all the help, discussions, laughs and general fun for the last six months. Finally, I would like to express my gratitude to Jonathan for giving me the opportunity to do a project in the group.



# Contents

Acknowledgements	iii
<b>1. Introduction</b>	<b>1</b>
<b>2. Theory</b>	<b>3</b>
2.1. The fundamentals of ion trapping . . . . .	3
2.1.1. Linear Paul trap . . . . .	3
2.1.2. Mathieu equation . . . . .	4
2.1.3. EMM due to RF phase mismatch . . . . .	5
2.2. Measuring micromotion . . . . .	7
2.2.1. Raman transitions and extracting the modulation index . . . . .	7
2.2.2. Numerical simulations for the modulation index . . . . .	8
2.2.3. Limitations, Raman scattering and decoherence . . . . .	9
2.3. Resonators . . . . .	10
2.3.1. Matching circuits . . . . .	11
<b>3. Electrode phase mismatch simulations</b>	<b>13</b>
3.1. Describing a Paul trap as a circuit . . . . .	13
3.1.1. Other RF and trap components . . . . .	13
3.1.2. Simulating a phase mismatch between electrodes . . . . .	14
<b>4. Two-phase resonator PCB</b>	<b>19</b>
4.1. Resonator PCB design . . . . .	19
4.2. Circuit simulations . . . . .	20
4.2.1. Ideal two-phase drive circuit model . . . . .	20
4.2.2. Resonator PCB - A realistic circuit model . . . . .	20
4.3. Assembling the new Resonator PCB . . . . .	24
4.3.1. Testing and comparing to simulations . . . . .	24
4.3.2. New RF amplifier . . . . .	26
<b>5. Micromotion measurements</b>	<b>29</b>
5.1. Beam-lines . . . . .	29
5.2. Measuring MM using stimulated Raman transitions . . . . .	29
5.2.1. Displacing the ion . . . . .	32
5.2.2. Extracting the modulation index, $\beta$ . . . . .	32
5.2.3. Comparing the sideband and time-tagging method . . . . .	36
<b>6. Conclusion and outlook</b>	<b>39</b>
<b>A. Coupled Oscillators</b>	<b>43</b>

*Contents*

<b>B. Deriving phase shift on electrodes</b>	<b>47</b>
<b>C. PCB components</b>	<b>51</b>

# List of Figures

2.1. Linear Paul trap . . . . .	5
2.2. Impedance matching networks . . . . .	11
3.1. Single- and two phase field lines in Paul trap . . . . .	14
3.2. Single-phase drive . . . . .	15
3.3. Phase mismatch on electrodes when changing $C_{phase}$ . . . . .	16
3.4. Phase mismatch on electrodes when changing $L_{phase}$ . . . . .	16
3.5. Phase mismatch on electrodes when changing a length of transmission line . . . . .	17
3.6. Phase mismatch on electrodes when changing resistance of feed-through . . . . .	17
4.1. Simplified two-phase LCR resonator . . . . .	21
4.2. Full LTspice circuit model . . . . .	23
4.3. Assembled resonator PCB . . . . .	24
4.4. New resonator testing, RF input . . . . .	25
4.5. New resonator testing, RF input . . . . .	26
4.6. New RF amplifier . . . . .	27
5.1. Beamlines in the molecule setup . . . . .	30
5.2. Motional sidebands and intercombinations . . . . .	31
5.3. EOM simulation . . . . .	32
5.4. Displacement a long radial x and y . . . . .	33
5.5. Measured modulation index . . . . .	34
5.6. DAC noise . . . . .	35
A.1. Coupled LCR oscillators . . . . .	43
A.2. Coupled LCR, out of phase drive . . . . .	45
A.3. Coupled LCR, in phase drive . . . . .	45
A.4. Coupled LCR, in phase drive . . . . .	46
A.5. Coupled LCR, phase synchronization . . . . .	46
B.1. Phase difference on electrodes . . . . .	47
C.1. PCB Schematic. . . . .	53



# List of Tables

4.1. RF amplifier specifications . . . . .	26
5.1. L-D parameters for Raman beams . . . . .	30
C.1. Components used in the new resonator PCB. . . . .	51
C.2. PCB trace parasitics . . . . .	52



# Introduction

---

Trapped ions are a widely recognized and established platform for quantum information processing [1] and well suited for metrology applications. Using the technique of quantum logic spectroscopy (QLS) measurements have been performed with atomic clocks [2, 3], and recent progress has been reported with molecular ions [4–6] as well as highly-charged ions [7]. The setup used in this thesis is designed to study  $\text{H}_2^+$  co-trapped with a  $\text{Be}^+$  ion using QLS [8].

The type of ion trap in this thesis is a Paul trap [9], which uses oscillating radio-frequency (RF) electric fields to provide a stable trap. A common issue in Paul traps is micromotion (MM), which arises when the ion experiences a residual RF field. Reducing MM is essential for precision measurements and spectroscopy, as it can lead to a second order Doppler shift (time dilation) that limits measurement precision [3, 10]. MM can be caused by stray electric fields or a phase mismatch on RF electrodes [10], caused by asymmetries in the resonator or trap wiring, such as different wire-length for different electrodes. In previous work, where a phase shift was introduced, the measured effect on the ion was much smaller than initially anticipated [11].

In this thesis, we study circuit simulations of the resonator, using LTspice. A resonator is used to achieve voltage amplification at the desired trap drive RF frequency and suppression of other frequency components. We use a lumped model element resonator, realized on a printed circuit board (PCB). In simulations we observe that the induced phase shift between electrodes is smaller than expected from simple assumptions about phase induced by transmission lines. The location of the asymmetry in the circuit model of the resonator is important. For our setup, the phase mismatch that arises between electrodes is much smaller when the wiring asymmetry is before the feed-through compared to close to the trap.

Based on this insight, a new version of a resonator PCB was developed. For the PCB the focus was on minimizing parasitics, i.e. unwanted circuit elements (inductance, capacitance and resistance). In particular, minimizing parasitic capacitance is essential. This ensures the capacitive load arises mainly from the trap which maximizes the voltage gain. The new resonator has a resonance frequency of  $\Omega_{RF,0}/2\pi = 78.71$  MHz and a voltage gain of  $G_V = 8.2$ . Another change made, in comparison to previous versions, was to use a high pass matching network. This led to improved suppression of low frequencies, especially around the motional frequencies of the trap, 1-10 MHz, which can otherwise lead to heating and decoherence [12].

Finally, a new beam-line was added to the setup to enable measurements of MM by driving the MM sideband using stimulated Raman transitions [2]. Using this one set of

## 1. Introduction

Raman beams, which couples to all three motional modes of a single  $\text{Be}^+$  ion, we measure a minimal modulation index of  $\beta = 0.11 \pm 0.01$ . We attribute this residual MM to the thermal motion of the ion cooled to the Doppler limit. Other limitations for these measurements were slow fluctuations in the voltages applied to the trap electrodes, displacing the ion by up to  $0.2 \mu\text{m}$  during measurement, also leading to a larger modulation index at the optimal point. Slow drifts in the MM compensated point were observed, due to electric patch potentials on the trap generated by UV lasers, high impedance shorts or drifts in the DAC supplying voltage to end-cap electrodes.

This thesis is structured as following. Chapter 2 introduces necessary theory to understand basics of ion trapping, resonators, MM and how to measure MM. In chapter 3 we investigate a single-phase drive trap model, using circuit simulations, and how a phase mismatch can arise if there is asymmetry in trap wiring. In chapter 4 we discuss the new resonator and deploy it in the lab, trapping a  $\text{Be}^+$  ion. Finally, in chapter 5 we measure MM by probing the MM sideband with stimulated Raman transitions.

# Theory

---

In this chapter we look at the fundamentals of trapping ions in a linear Paul, focusing on how a phase mismatch on the trap RF electrodes can cause excess micromotion (EMM). To measure MM we introduce a method where the MM sideband is driven using stimulated Raman transitions. The last part of the chapter introduces resonators and why they are used in Paul traps.

## 2.1. The fundamentals of ion trapping

The first challenge for trapping a charged particle in three dimensional space is Laplace's equation [13, 14]:

$$\frac{\partial^2 \phi}{\partial x^2} + \frac{\partial^2 \phi}{\partial y^2} + \frac{\partial^2 \phi}{\partial z^2} = 0 \quad (2.1)$$

where the potential  $\phi(x, y, z)$  is of the form,

$$\phi(x, y, z) = \alpha x^2 + \beta y^2 + \gamma z^2 \quad (2.2)$$

The Laplace's equation can e.g. be fulfilled with having all three parameters,  $\alpha = \beta = \gamma = 0$ , but that does not lead to stable trapping. Another possibility is  $-\alpha = -\beta = 2\gamma$  where there is confinement along z but anti-confinement along x- and y. Hence, we cannot use only static electric field to trap in three dimensions.

We therefore look at one possible way of trapping charged particles, where the trap used is commonly known as a Paul trap and uses RF electric fields along with DC fields to achieve stable trapping conditions. Another possible implementation, which does not use RF fields but rather DC electric fields and a magnetic field are Penning traps [15].

### 2.1.1. Linear Paul trap

In linear Paul trap [9] the electric potential takes the form [13]

$$\phi(x, y, z) = \frac{1}{2}U_{dc}(\alpha_{dc}x^2 + \beta_{dc}y^2 + \gamma_{dc}z^2) + \frac{1}{2}U_{rf}\cos(\Omega_{rf}t)(\alpha_{rf}x^2 + \beta_{rf}y^2 + \gamma_{rf}z^2) \quad (2.3)$$

which has a DC (static) and an RF (oscillating) term and where  $U_{dc}$  and  $U_{rf}$  are the voltages on the dc and RF electrodes respectively and  $\Omega_{RF}$  is the RF drive frequency.

## 2. Theory

One can tailor the trap geometry such that  $-\frac{1}{2}\alpha_{dc} = -\frac{1}{2}\beta_{dc} = \gamma_{dc}$  and  $\alpha_{rf} = -\beta_{rf}$ ,  $\gamma_{rf} = 0$ , noting that the Laplace's equation is fulfilled.

Fulfilling the Laplace equation is not sufficient to ensure a stable trap in three dimensions. For that we need to tailor the range of parameters in eq. 2.3. To analyze, we look at the force on the ion and solve the equation of motion (EOM) which takes the form of what is commonly known as the Mathieu equation.

### 2.1.2. Mathieu equation

With  $u = x, y, z$  and  $\delta_{dc/rf} = \{\alpha_{dc/rf}, \beta_{dc/rf}, \gamma_{dc/rf}\}$ , we start with the EOM, given by [13]

$$\frac{d^2u}{dt^2} = -\frac{Ze}{m} \frac{\partial \phi}{\partial u} = \frac{Zeu}{m} (U_{dc}\delta_{dc} + U_{rf}\delta_{rf}\cos(\Omega_{rf}t)) \quad (2.4)$$

where  $Z$  is the ion's charge number,  $e$  elementary charge and  $m$  the ion's mass. The standard form of the Mathieu equation is [16]

$$\frac{d^2u}{dt^2} = (a_u + 2q_u\cos(2\zeta))u \quad (2.5)$$

To get this form we introduce the a- and q-parameters,

$$a_u = \frac{4ZeU_{dc}\delta_{dc}}{m\Omega_{rf}^2} \quad (2.6)$$

$$q_u = \frac{2ZeU_{rf}\delta_{rf}}{m\Omega_{rf}^2} \quad (2.7)$$

and set

$$\zeta = \Omega_{rf}t/2$$

The Mathieu equation has a known solution of the form [13, 16],

$$u(\zeta) = A\exp(i\beta_u\zeta) \sum_n C_{2n}\exp(i2n\zeta) + B\exp(-i\beta_u\zeta) \sum_n C_{-2n}\exp(-i2n\zeta) \quad (2.8)$$

where  $A$  and  $B$  are constants and for a stable trap  $\beta_u \in \{0, 1\}$

Assuming  $|a_{x,y,z}|, q_{x,y}^2 \ll 1$ , which is a range we try to work in by choosing trap voltages and RF drive frequencies, the first order approximate solution is

$$u(t) = A\cos(\omega_u t) \left( 1 - \frac{q_u}{2} \cos(\Omega_{rf}t) \right) \quad (2.9)$$

The motion of the ion is governed by two frequencies, the secular motion with frequency  $\omega_{u,sec}$ , referred to as the *trap frequency*. For each spatial direction the ion sees a harmonic potential. For the axial direction, z, the trap frequency is given by

## 2.1. The fundamentals of ion trapping

$$\omega_z = \sqrt{a_z} \frac{\Omega_{rf}}{2} = \sqrt{\frac{ZeU_{dc}\gamma_{dc}}{m}} \quad (2.10)$$

and for the radial directions,  $x$  and  $y$ , they are

$$\omega_{x,y} = q_{x,y} \frac{\Omega_{rf}}{2\sqrt{2}} = \frac{ZeU_{rf}\delta_{rf}}{\sqrt{2}m\Omega_{rf}} \quad (2.11)$$

These expressions for the trap frequencies neglect effects from the static potential on the radials and from the RF on the axial [13].

The frequency component at  $\Omega_{rf}$  is the *RF drive frequency*. This is the frequency at which we generate the oscillating voltages on the RF trap electrodes. The fast motion on top of the harmonic oscillation that arises due to the RF drive is called micromotion (MM). Averaging over the MM gives a pseudopotential which looks like a static potential [13]. We typically distinguish contributions to the micromotion: *intrinsic* and *excess* micromotion, IMM and EMM respectively. EMM is e.g. due to electric stray fields in the trap. These stray fields displace the ion such that it feels a residual RF field away from the trap center causing larger MM. Another possible cause of EMM is a phase mismatch on the RF electrodes. This could e.g. arise if the propagation delay is different for different RF electrodes due to asymmetric wiring in the trap [10]. Example of IMM is e.g. due to imperfect trap geometry, where misaligned RF electrodes cause an imperfect quadrupole field such that there is always some residual RF field.

### 2.1.3. EMM due to RF phase mismatch

Figure 2.1 shows a typical four-rod Paul trap. We now assume a phase difference,  $\phi_{mismatch}$ , introduced between the two RF electrodes, with the other two grounded.

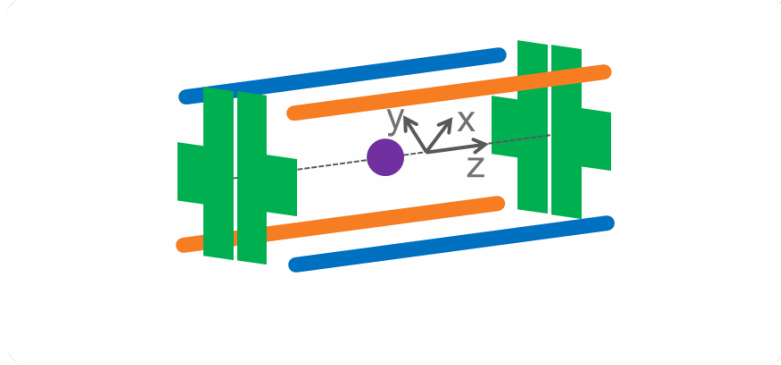


Figure 2.1.: A Linear Paul trap. There are four RF electrodes (blue and orange) and four DC end-cap electrodes (green). Credit: Nick Schwegler

On one RF electrode we can write the voltage  $U_{rf}\cos(\Omega_{rf}t + \frac{1}{2}\phi_{mismatch})$  and for the other  $U_{rf}\cos(\Omega_{rf}t - \frac{1}{2}\phi_{mismatch})$

Assuming the phase mismatch is small,  $\phi_{mismatch} \ll 1$ , we can expand [10]

## 2. Theory

$$U_{rf}\cos(\Omega_{rf}t + \frac{1}{2}\phi_{mismatch}) \approx U_{rf}\cos(\Omega_{rf}t) - \frac{1}{2}U_{rf}\phi_{mismatch}\sin(\Omega_{rf}t) \quad (2.12)$$

and

$$U_{rf}\cos(\Omega_{rf}t - \frac{1}{2}\phi_{mismatch}) \approx U_{rf}\cos(\Omega_{rf}t) + \frac{1}{2}U_{rf}\phi_{mismatch}\sin(\Omega_{rf}t) \quad (2.13)$$

The second term containing  $\sin(\Omega_{rf}t)$  terms introduces additional oscillating electric field which can be approximated as an electric field from a parallel plate capacitor with spacing  $2R/\alpha$ , where  $\alpha$  is a geometrical constant which depends on trap geometry and  $R$  is the distance from the ion to the electrode [10].

To estimate the correction factor,  $\alpha \in \{0, 1\}$ , where  $\alpha = 1$  is the case of a ideal plate capacitor, we can use finite element simulations of the electric potential and electric fields in the ion trap. Then, we compare the field from simulations to a value from a plate capacitor. Assuming  $E_{simulation} = V\alpha/R$  where  $E_{simulation}$  is the value from trap simulations we obtain the correction factor by

$$\alpha = \frac{E_{simulation}}{V/d} = \frac{E_{simulation}}{E_{platecap}} \quad (2.14)$$

where  $d$  is the spacing of the plate capacitor.

The value for an electric field at the trap center, if there is a phase mismatch, is

$$E = \frac{U_{rf}\phi_{mismatch}}{2R/\alpha} \cdot \sin(\Omega_{rf}t) \quad (2.15)$$

Then also making the further assumption that  $\delta_{rf} = 1/R^2$  [10] we arrive at an expression for the electric field,

$$E = \frac{U_{rf}R\alpha\phi_{mismatch}}{2R^2} \cdot \sin(\Omega_{rf}t) = \frac{U_{rf}R\alpha\phi_{mismatch}\delta_{rf}}{2} \cdot \sin(\Omega_{rf}t) \quad (2.16)$$

This leads to an additional force on the ion according to  $F = -eZ \cdot E$ .

Adding this additional electric field due to a phase mismatch to the EOM (eq. 2.4) yields, with same definition for a- and q-parameters (eq. 2.6 and 2.7) and  $\zeta$  (eq. 2.1.2)

$$\frac{d^2u}{d\zeta^2} = (a_u + 2q_u\cos(2\zeta))u - \underbrace{\frac{4}{\Omega_{rf}^2} \frac{ZeU_{rf}\delta_{rf}}{2m} R\alpha\phi_{mismatch}}_{q_u} \cdot \sin(2\zeta) \quad (2.17)$$

Again solving the Mathieu equation to lowest order, similar to eq. 2.9, with this added driving term we arrive at

$$u(t) = A\cos(\omega_u t) \left(1 - \frac{q_u}{2}\cos(\Omega_{rf}t)\right) - \frac{1}{4}q_u R\alpha\phi_{mismatch}\sin(\Omega_{rf}t) \quad (2.18)$$

## 2.2. Measuring micromotion

Several methods can be used to measure micromotion. The two methods discussed here are photon time-tagging and Raman spectroscopy [10, 17]. Photon time-tagging relies on correlating the arrival times of the photons to the RF cycle. When using a beam, detuned from an electronic transition, the MM leads to Doppler shifts and therefore change in fluorescence, correlated to the RF signal. The photon time-tagging method was previously used to measure MM in the molecule setup [11]. In this thesis we expand on these measurements and use stimulated Raman transitions to measure MM using the sideband method. We note that to gain information about MM in all three spatial directions we need three sets of laser beams to drive the Raman transitions. A single beam can have a projection on all three normal modes of the ion but for the full picture we need three independent set of beams. They don't need to be orthogonal but must span a three dimensional space.

### 2.2.1. Raman transitions and extracting the modulation index

For the sideband method we drive stimulated, two photon, Raman transitions using two laser beams. These beams have some common large detuning,  $\Delta$ , from a dipole transition. They also have a slight relative detuning,  $\delta$ , from each other which can be changed using e.g. an acousto-optic modulator (AOM). By changing this relative detuning we can match the frequency spacing of a hyperfine qubit in  $\text{Be}^{9+}$  and drive carrier transitions, as well as motional sideband transitions. Similarly, we can also drive MM sideband transitions at  $+/- n\Omega_{RF}$  away from the carrier frequency, where n is an integer.

Being able to drive both the carrier and MM sideband one can extract the modulation index,  $\beta$ , which is a laser phase modulation arising from first order Doppler shift due to the periodic MM with velocity,  $\vec{v} = \vec{v}_0 \cos(\Omega_{RF}t)$  [17]

$$\beta = \frac{\vec{k} \cdot \vec{v}_0}{\Omega_{RF}} \quad (2.19)$$

The modulation index then gives information about the amplitude of the MM along the k-vector of the laser. To measure  $\beta$  one can measure the ratio of the Rabi rate of the carrier,  $\Omega_C$ , and the MM sideband,  $\Omega_{MM}$ . The ratio is

$$\frac{\Omega_{MM}}{\Omega_C} = \frac{J_1(\beta)}{J_0(\beta)} \approx \frac{\beta}{2} \quad (2.20)$$

where  $J_1(\beta)$  and  $J_0(\beta)$  are Bessel functions. Assuming  $\beta \ll 1$ , we can expand the Bessel functions for a simple expressions of the modulation index [17].

Assuming there is a point in the trap where there are no residual RF fields the ion has no MM and therefore the modulation index goes to zero. However, due to thermal motion of the ion we can still expect to observe the MM sideband even when the ion sits at this point. For a Fock state with n phonons this thermal effect can yield a Rabi rate ratio as big as [17]

## 2. Theory

$$\left| \frac{\Omega_{MM}}{\Omega_C} \right| = \frac{q_i}{4} \eta_i^2 (2n + 1) + O(\eta_i^4) \quad (2.21)$$

Assuming Doppler cooling the theoretical temperature reached is the Doppler limit [10, 13]

$$T_{Doppler} \approx \frac{\hbar\Gamma}{2k_B} \quad (2.22)$$

where  $\Gamma$  is the linewidth of the cooling transition.

A thermal state of the ion, assuming a harmonic potential, with certain temperature will then be a statistical mixture of Fock states,  $|n\rangle$ , which are weighted by

$$P_n = \frac{\bar{n}^n}{(\bar{n} + 1)^{n+1}}$$

where  $\bar{n}$  is the average phonon number [18].

$$\bar{n} = \frac{1}{\exp(\frac{\hbar\omega_u}{k_B T}) - 1}$$

The time-averaged position is then a Gaussian distribution, assuming  $k_B T \gg \hbar\omega_u$ , with an RMS width of [18, 19]

$$\Delta u = \sqrt{\frac{k_B T}{m\omega_u^2}} \quad (2.23)$$

Now taking a weighted average of 2.21 for a thermal state we can give an upper bound for the ratio of the MM sideband to the carrier, and hence the modulation index.

$$\left| \frac{\Omega_{MM}}{\Omega_C} \right|_{thermal} \approx \sum_n P(n) \frac{q_i}{4} \eta_i^2 (2n + 1) \quad (2.24)$$

The drawback of the sideband method is that we cannot distinguish between EMM arising from static fields causing displacement or from electrode phase mismatch. The time-tagging method can achieve this [17].

### 2.2.2. Numerical simulations for the modulation index

To compare to the measured modulation index we can simulate it by using the solution to the ion EOM, eq. 2.4. Then we calculate the electric field of the laser in the rest frame of the ion [10]

$$E(t) = E_0 \exp(i\vec{k}_u \cdot \vec{u}(t) - i\omega_{laser}t + \phi) \quad (2.25)$$

Ultimately we are interested in the electric field intensity

$$|\tilde{E}(\omega)|^2 \quad (2.26)$$

because the Rabi rate is proportional to the electric field,  $\Omega_{Rabi} \propto E$ , which we can use to get the phase modulation index,  $\beta$ .

$$\beta \approx 2 \frac{\Omega_{MMsideband}}{\Omega_{carrier}} = 2 \frac{|\tilde{E}_{MMsideband}|}{|\tilde{E}_{carrier}|} \quad (2.27)$$

Numerically solve the ion EOM for given a- and q- parameters of the trap we extract the modulation index by calculating the exponent in 2.25 and Fourier transforming. As we are interested in the ratio of the electric field intensity for the carrier and MM sideband,  $E_0$  does not matter.

Another way to extract the modulation index by simulation is to calculate the residual RF field,  $E_{RF}$ , in the trap using finite element simulations. From the residual RF field the modulation index is [17],

$$\beta = \frac{kQ E_{RF}}{m\Omega_{rf}^2} \quad (2.28)$$

where  $Q$  ion charge,  $m$  ion mass and  $k$  the component of the  $\vec{k}$ -vector parallel to  $E_{RF}$ .

### 2.2.3. Limitations, Raman scattering and decoherence

The two beams used for the Raman transitions can not be infinitely detuned from the dipole transition as the transitions would become infinitely slow and qubit coherence becomes the limiting factor. A finite detuning means there is always some possibility of scattering photons which can lead to two different outcomes. First is a phase-reset if the electron decays to the level it started from and is called Rayleigh scattering. The second is a spin-flip if it decays to the other qubit level and is called Raman scattering [13].

The Rabi frequency for the Raman transition is [13]

$$\Omega_{Raman} \approx \frac{\Omega_1 \Omega_2}{\Delta}$$

where  $\Omega_1$  and  $\Omega_2$  are the Rabi rates for the dipole transitions of beam 1 and 2. The scattering rate for the Raman transition is [13]

$$\Gamma \approx \frac{\Gamma_{dip}(\Omega_1^2 + \Omega_2^2)}{\Delta^2}$$

where  $\Gamma_{dip}$  is the scattering rate of the bare dipole transition. Thus, in order to maximize the Rabi frequency while keeping the scattering rate as small as possible we want beams of equal strength, i.e.  $\Omega_1 = \Omega_2$ .

## 2. Theory

### 2.3. Resonators

To trap the ion we need to apply an oscillating voltage to the trap electrodes with a single frequency component. For typical trap geometries and desired secular frequencies, the required RF voltage needs to be amplified. To amplify the RF voltage coming from an RF source and at the same time achieve high spectral isolation, resonators are used. Different types of resonators have been used for ion traps [12]. In this work we focus on lumped model LCR resonators. In the simplest case it is made up of, as the name suggests, a resistor ( $R$ ), a coil ( $L$ ) and a capacitor ( $C$ ). A simple LCR resonator achieves the criteria of amplifying the voltage at the resonance frequency,  $\Omega_0$ , and suppressing it for other frequencies.

For an LCR resonator the resonance frequency is

$$\Omega_0 = \frac{1}{\sqrt{LC}} \quad (2.29)$$

For a series LCR resonator the voltage gain is the ratio between the output and input voltage and given by [12]

$$G_V = \frac{V_{out}}{V_{in}} = \frac{1}{R} \sqrt{\frac{L}{C}} \quad (2.30)$$

If there is a mismatch in the source impedance,  $Z_S$ , and the resonator impedance,  $R$ , which is usually the case for ion trap drives, we get a slightly modified expression

$$G_V^M = \sqrt{\frac{L}{Z_S RC}} = \frac{\omega_0 L}{\sqrt{Z_S R}} \quad (2.31)$$

To maximize the gain, for a given resonance frequency  $\Omega_0$ , we want to minimize the capacitance and maximize the inductance.

The quality factor,  $Q$ , of a resonator is [12]

$$Q = 2 \frac{\Omega_0}{\Delta\Omega_V} \quad (2.32)$$

where  $\Delta\Omega_V$  is the -3dB bandwidth.

A higher  $Q$  factor means higher gain and better spectral isolation, a desirable trait for the resonator. Lumped model resonators typically have lower  $Q$  compared to helical resonators [12] but the advantage of using a lumped model element resonator built from discrete components on a PCB is the high level of flexibility, i.e. being able to add functionality on the PCB and adjust the resonance frequency by exchanging simple components.

As the the source and load will not be matched we now take a look at matching networks. They are essential in ensuring optimal voltage gain on the trap electrodes.

### 2.3.1. Matching circuits

One way to achieve matching is to use a transformer. These are not considered viable for ion trap drives in general as they can only be bought in set values for winding ratios, and can therefore not be used to match arbitrary loads to a  $50\Omega$  source. Another possibility are L-section networks. Different configurations of L-matching networks exist. These can be used to match arbitrary value of loads to arbitrary values of source<sup>i</sup>. The chosen matching network depends on whether the load is larger or smaller than the source and whether we want a low-pass or a high-pass characteristics. Typically, we can have four configurations seen in figure 2.2, two where the load is larger than the source,  $R_L > R_S$ , and two where the load is smaller than the source,  $R_L < R_S$ . Ideally, the resonator has a low resistance so we consider the latter case. Then the question is whether one wants low-pass or high-pass filtering. For ion trapping, the high-pass is desirable as lower frequency components can introduce noise close to the trap frequencies,  $\omega_{x,y,z}$ , which are on the order of a few hundred kHz to a few MHz. This leaves us with case (d) in figure 2.2 where there is an inductor to ground followed by a capacitor in series.

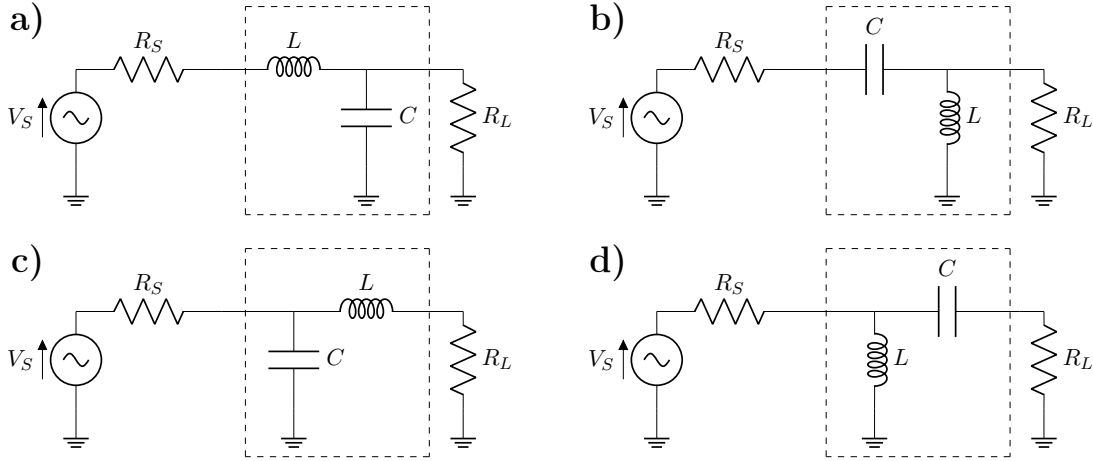


Figure 2.2.: Four different types of L-section matching networks. The choice of which network depends if up-converting is needed, i.e.  $R_L < R_S$  (**c** or **d**) or down-converting,  $R_L > R_S$  (**a** or **b**). Then in both cases one can choose a high-pass filter (**b** and **d**) or low-pass filter (**a** and **c**) characteristics of the matching network.

<sup>i</sup>When the load and source have very different impedance values the Q-factor of the match needs to be very high, which also decreases the bandwidth. For this, cascaded L-section networks can be used.



# Electrode phase mismatch simulations

---

As a phase mismatch on the trap electrodes can cause EMM [10], as seen in section 2.1.3, we want to know how large the phase mismatch is that arises due to asymmetries in the trap wiring. For that we need a simple circuit model for a Paul trap and other components in the RF circuitry. We then investigate the induced phase and voltage mismatch of the electrodes when asymmetry is introduced in the circuit model.

## 3.1. Describing a Paul trap as a circuit

In this thesis we focus on a four-rod linear Paul trap, which is a common way of building an ion trap and used in the molecule experiment. These trap rods have some distance from each other, and being metallic with some spacing they have some capacitance. Looking at the case of the single phase-drive, two electrodes have an applied RF voltage while the other two are grounded, as seen in figure 3.1. This is represented in a circuit model in figure 3.2, where each RF electrode has a capacitor to ground and a capacitor between the two.

Another possibility, also seen in figure 3.1, for connecting the RF signal to the electrodes is to drive all four but in two pairs, RF+ and RF-. One pair is then 180 degree phase shifted compared to the other. We refer to this a two-phase drive. In the case of the molecule setup we have a two-phase drive. The two-phase drive can lower residual RF fields along the axial, z, normal mode, leading to lower MM [20].

### 3.1.1. Other RF and trap components

We divide the RF circuitry into the five segments, seen in figure 3.2. First there is the  $50\Omega$  RF source,  $V_{RF}$ , followed by the resonator PCB. Then there is the feed-through, long metallic rods that connect to a PCB which sits in vacuum. Finally, there is the trap. The component values for the circuit model are based on the Paul trap used in the molecule setup. With everything symmetric the values of the feed-through inductance are to  $L_1 = L_2 = 100\text{nH}$ , the trap capacitance  $C_1 = C_2 = 4.4\text{pF}$  and  $C_c = 2.2\text{pF}$  and resistance  $R_1 = R_2 = 0.5\Omega$ . The resonator coil is  $L_{res} = 370\text{nH}$  with resistance  $R_{res} = 0.5\Omega$ . The trap capacitance is  $C_{1,trap} = C_{2,trap} = 0.2\text{pF}$  and  $C_{trap,c} = 0.1\text{pF}$ . With this circuit model we can now simulate a phase mismatch between electrodes when

### 3. Electrode phase mismatch simulations

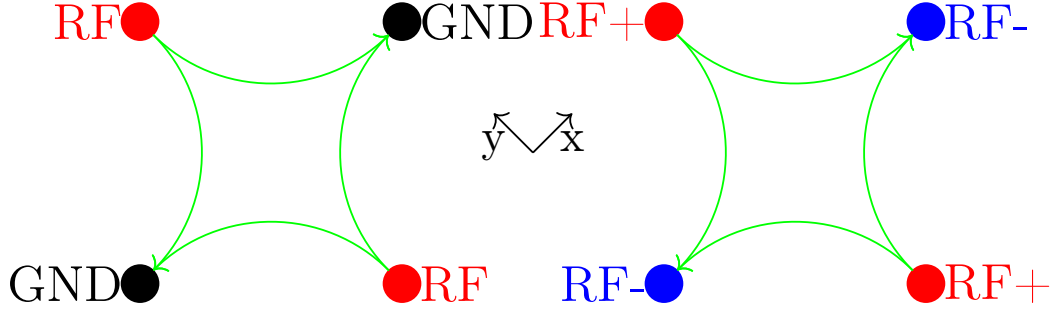


Figure 3.1.: Single vs two-phase drive in a linear Paul trap. RF field lines in the radial, x-y, plane at one point in time. For the single-phase drive RF voltage is only applied on two of the four electrodes. For the two-phase drive the two pairs, RF<sub>+</sub> and RF<sub>-</sub>, are driven 180 degrees phase shifted from one another.

wiring assymetry arises.

#### 3.1.2. Simulating a phase mismatch between electrodes

We look at two cases of trap wiring asymmetry and simulate the resulting phase and voltage mismatch on the trap electrodes. Firstly, adding extra wire length before the feed-through. This amounts to what was done in previous work using SMA phase-shifters [11], where the wire length of one of the SMA cables connected to the feed-through rods was longer than the other three. The difference in path length was  $\Delta l = 2.2\text{mm}$ . A typical  $50\Omega$  coax cable<sup>i</sup> has a capacitance per unit length of  $100\text{pF/m}$  and inductance per unit length of  $250\text{nH/m}$ . These value give a characteristic impedance  $Z_{char} = \sqrt{L/C} = 50\Omega$  [21]. To model the SMA cable we use a lumped transmission line model [21], adding a single coil followed by a capacitor to ground. Thus, for an added length of  $2.2\text{mm}$  we have a lumped model with  $L_{phase} = 0.54\text{nH}$  and  $C_{phase} = 0.22\text{pF}$ . The second case is where some asymmetry arises before the trap. This could e.g. be the case if the wire-bonding connecting the vacuum PCB to the trap is not the same for all electrodes, adding inductance. Another possibility is if some wiring passes close to a ground plane, adding capacitance. For comparison we place the same lumped-model of the phase-shifter in both locations, i.e. before the feed-through coils and before the trap. Assuming a drive frequency of  $\Omega_{RF}/2\pi = 80\text{MHz}$  such a SMA cable adds a phase shift of  $\phi_{mismatch} = 0.317$  degrees for a matched system.

Having added this to the circuit model, we simulate three cases. First, changing only the capacitor,  $C_{phase}$  with  $L_{phase}$  fixed. Then, changing only the inductor,  $L_{phase}$  with  $C_{phase}$  fixed. Finally we change both at the same time. All simulations are made with a RF frequency of  $\Omega_{RF}/2\pi = 80\text{MHz}$ .

<sup>i</sup>RG-58, has a propagation velocity of  $v \approx (2/3) \cdot c$  [21], where  $c$  is the velocity of light in vacuum.

### 3.1. Describing a Paul trap as a circuit

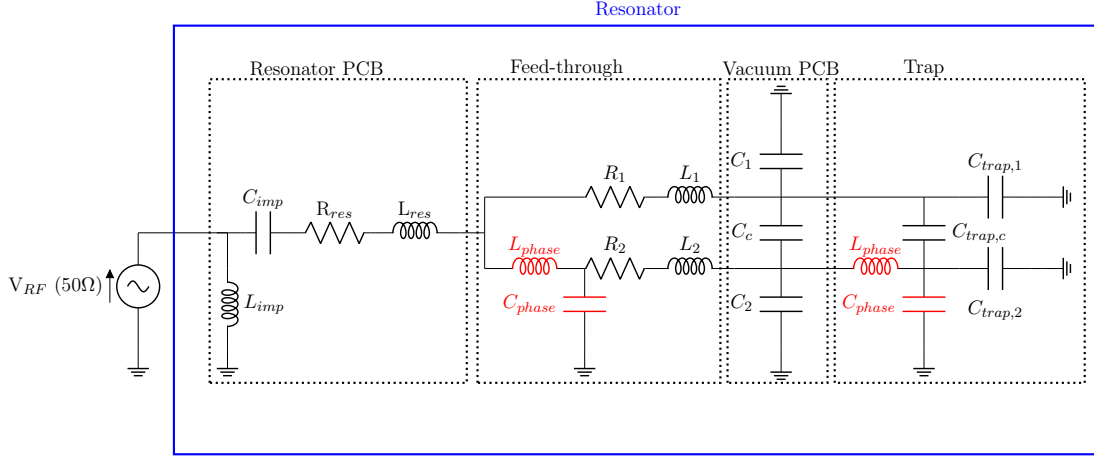


Figure 3.2.: A circuit model for the single phase trap drive RF circuitry. The RF voltage signal comes from the RF source,  $V_S$ , connected to a Resonator PCB which houses the matching network,  $L_{imp}$  and  $C_{imp}$ , a resonator coil,  $L_{res}$ , that has some parasitic resistance,  $R_{res}$ . The output of the resonator PCB then connects to the feed-through, metallic rods which are modelled by coils,  $L_1$  and  $L_2$ , with parasitic resistance,  $R_1$  and  $R_2$ . Next is another, in-vacuum PCB, where the main capacitance contribution comes from,  $C_1$  and  $C_2$  to ground and  $C_c$  between the signal traces. Finally there is the trap, also modelled by capacitance to ground,  $C_{trap,1}$  and  $C_{trap,2}$  and between the electrodes,  $C_{trap,c}$ . The combination of resonator PCB, feed-through, vacuum-PCB and the trap is referred to as the resonator.

The case where the capacitance  $C_{phase}$ , changes with the inductance fixed,  $L_{phase} = 0\text{nH}$  is depicted in figure 3.3. The added capacitance adds considerably more phase shift when placed before the trap with negligible effects if placed before the feed-through.

Figure 3.4 shows what happens when the inductor,  $L_{phase}$ , is changed with the capacitance fixed at  $C_{phase} = 0\text{pF}$ . The phase and voltage mismatch is higher when added before the feed-through but still the effect is small.

Changing both values,  $L_{phase}$  and  $C_{phase}$ , simultaneously in figure 3.5, simulates an added length of a coaxial cable, keeping the characteristic impedance fixed at  $50\Omega$ . When placed before the feed-through the phase mismatch for a 2.2 mm long SMA is 0.0003 degrees and before the trap it is 0.01 degrees, compared to an expected phase mismatch of 0.317 degrees, in a matched system. Avoiding asymmetries, close to the trap in our case, is therefore more important than before the feed-through.

Finally, in figure 3.6, we change the value of the feed-through resistance,  $R_1$  and  $R_2$  simultaneously for a cable length of 2.2mm and drive frequency of 80MHz. For a small phase mismatch it increases linearly with increased resistance. We also see that if there is no resistance there is no phase mismatch. For the voltage ratio there is no change when the resistance changes. For a simpler model, where we can easily solve for the phase

### 3. Electrode phase mismatch simulations

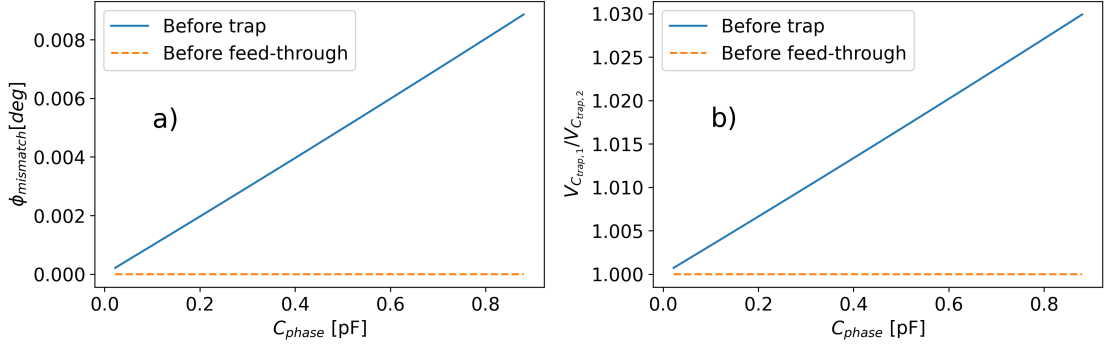


Figure 3.3.: Changing the capacitor  $C_{\text{phase}}$  in the circuit model of a single-phase drive trap, before the feed-through and before the trap. The value of the inductor is  $L_{\text{phase}} = 0\text{nH}$ . Drive frequency is  $\Omega_{RF}/2\pi = 80\text{MHz}$ . **a)** Induced phase mismatch on the electrodes. A bigger effect is seen when placing the capacitor before the trap. **b)** Voltage ratio on the electrodes. A bigger effect is seen when placing the capacitor before the trap.

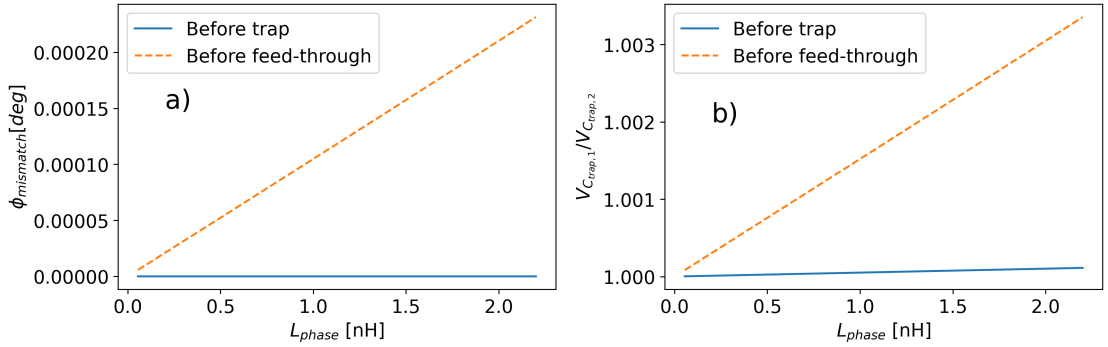


Figure 3.4.: Changing the inductor  $L_{\text{phase}}$  in the circuit model of a single-phase drive trap, before the feed-through and before the trap. The value of the capacitor is  $C_{\text{phase}} = 0\text{nH}$ . Drive frequency is  $\Omega_{RF}/2\pi = 80\text{MHz}$ . **a)** Induced phase mismatch on the electrodes. A bigger effect is seen when placing the inductor before the feed-through. **b)** Voltage ratio on the electrodes. A bigger effect is seen when placing the inductor before the feed-through.

mismatch analytically between electrodes and how it arises, see appendix B.

These results can be extended to the two-phase drive as well, where the phase mismatch arises between electrodes with same polarity.

### 3.1. Describing a Paul trap as a circuit

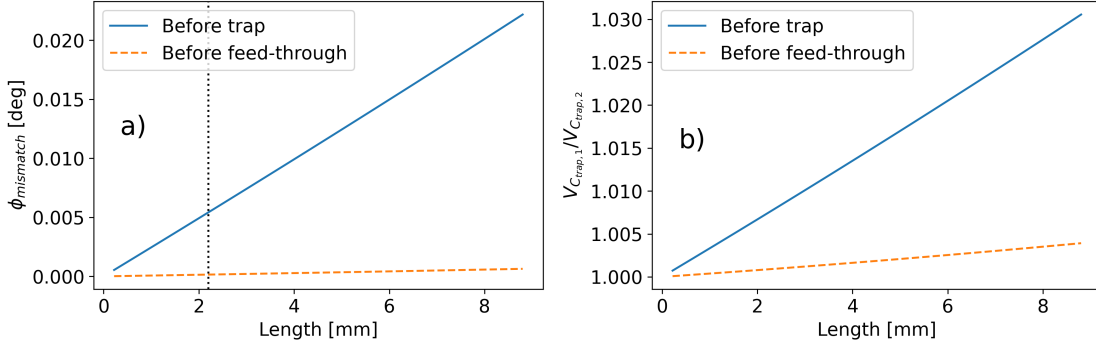


Figure 3.5.: Changing the inductor  $L_{\text{phase}}$  and capacitor  $C_{\text{phase}}$  in the circuit model of a single-phase drive trap, before the feed-through and before the trap. This equals the effect of changing the length of  $50\Omega$  transmission line. Drive frequency is  $\Omega_{RF}/2\pi = 80\text{MHz}$ . **a)** Induced phase mismatch on the electrodes. A bigger effect is seen when placing the inductor before the feed-through. In both cases the phase mismatch is much smaller than induced by transmission line of length 2.2mm in a matched system. **b)** Voltage ratio on the electrodes. A bigger effect is seen when placing the inductor before the feed-through.

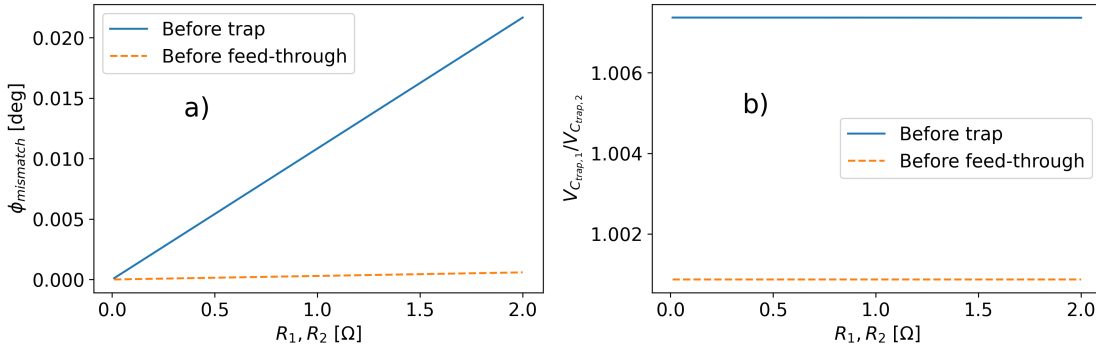


Figure 3.6.: Changing the resistance of the feed-through with fixed values of  $L_{\text{phase}}$  and  $C_{\text{phase}}$  corresponding to a SMA of length 2.2mm, before the feed-through and before the trap. Drive frequency is  $\Omega_{RF}/2\pi = 80\text{MHz}$ . **a)** Induced phase mismatch on the electrodes. To induce a phase mismatch, the feed-through must have a resistive component. **b)** Voltage ratio on the electrodes. For a fixed length, the resistance of the feed-through does not change the voltage ratio.



# Two-phase resonator PCB

---

For this project a new iteration of the molecule resonator PCB was developed and produced. The motivation for a new iteration was to achieve higher voltage gain at higher trap drive frequency. Increasing the gain allows for a better RF amplifier with a lower noise figure (NF). In chapter 3 we saw that the phase-shifters from previous version are no longer needed. A final motivation is to improve noise isolation at low frequencies, around ion(s) motional frequencies. These improvements should lead to better motional coherence and improved heating rates [12], which is important as the next step for the molecule step involves investigating weakly coupled radials of the Be-H<sub>2</sub> crystal [8].

## 4.1. Resonator PCB design

Iterative upgrades were made to the resonator PCB design combining knowledge from previous versions [11, 22]. The priority for this version was to minimize parasitics originating from the PCB, in particular the parasitic capacitance. Ideally, the trap is the dominating capacitive load, or at least of the same order of magnitude as the PCB. As shown in eq. 2.31 the voltage gain, for a fixed resonance frequency, is maximized when we minimize the capacitive load.

In summary, the following changes were implemented:

1. Minimize all parasitics; L, C and R:
  - Focus on minimizing parasitic capacitance. *Can e.g. be done by reducing trace width on the PCB but that comes at the cost of increasing L and R.*
  - Use a two-layer PCB with a single ground plane. Previous PCB used four-layers [11]. *Decreases C but increases L.*
  - Minimize the layout and distances on the PCB and try to make all tracks shorter. *Minimizes L, C and R.*
  - Remove SMA connectors that connect PCB to feed-through. Go for pins as in the original design [22]. *Decreases L, C and R.*
2. Use a high-pass L-matching network (see section 2.3.1):
  - Better low-frequency filtering of the RF input.
3. Make components footprints more modular:

#### 4. Two-phase resonator PCB

- Choose a resonator coil which has the same footprint for different values of inductance. *This gives the possibility of tuning the resonance frequency in retro respect without having to include a large pad to account for different sizes. Smaller pads mean less parasitics*
- Same for the coil in the matching network and all capacitors and resistors, use a common footprint.

### 4.2. Circuit simulations

Before producing the newest version of the resonator PCB, simulations were made to investigate circuit behaviour, most importantly the resonance frequency and voltage gain. We start by building a model of the circuit for the simplest two-phase LCR-resonator before adding complexity and arriving at the final design. We start with a similar model as in chapter 3 except adding the two phase drive. All circuit simulations were made in LTspice<sup>i</sup>, a SPICE based analog electronic circuit simulator.

#### 4.2.1. Ideal two-phase drive circuit model

Figure 4.1 illustrates the simplest model of the two phase resonator. For simplicity we neglect the feed-through and the vacuum PCB for the moment. The input signal from the RF source is converted from a single phase input to a balanced dual phase output using a balun<sup>ii</sup>. We denote these branches, which have the same voltage but are 180 degrees out of phase, RF+ and RF-. Each branch has a matching network, a resonator coil  $L_{res}$  and resonator resistance,  $R_{res}$ . As with the single phase drive the trap is modelled as a capacitor,  $C_{trap}$ .

#### 4.2.2. Resonator PCB - A realistic circuit model

Whilst the model in figure 4.1 is the simplest case of our setup it disregards any parasitic effects and other components of the PCB. We therefore extend the model to include this in simulations. To do so we calculate the parasitics based on the geometry and material properties of the PCB, the feed-through and the trap. For the frequencies involved,  $\Omega_{RF} \leq 100$  MHz, and the length of the traces  $l \approx 1 - 10$ cm we use a lumped model for each segment [21, 23]. A general rule of thumb of when this is applicable is that the ratio of trace length,  $l$ , versus wavelength,  $\lambda$ , is less or equal than 10,  $l/\lambda < 10$  [21, 23]. This means each segment is a coil and a resistor in series followed by a capacitor to ground, also known as a lumped transmission line model [21]. When modelled as a simple capacitor, the best estimate for the trap capacitance is  $C_{trap} = 8.8$  pF. Figure 4.2 shows the full circuit model for the resonator including parasitics, highlighted with red dotted squares, and the other components, namely the capacitive dividers and bias-tee.

---

<sup>i</sup><https://www.analog.com/en/design-center/design-tools-and-calculators/ltspice-simulator.html>

<sup>ii</sup>balun: "balanced to unbalanced"

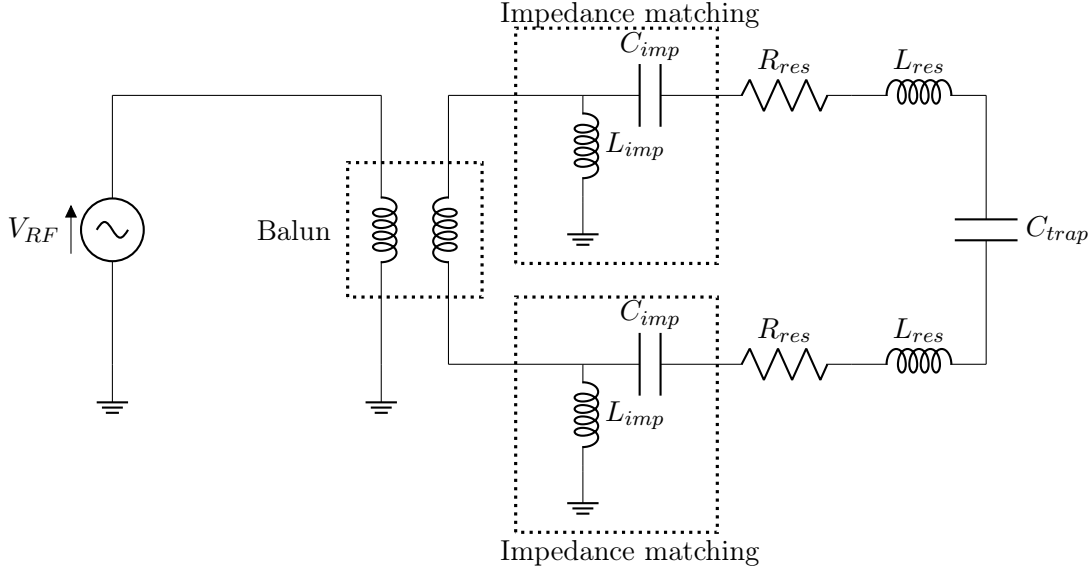


Figure 4.1.: Simplified model of a two-phase LCR resonator. A balun takes the input signal and converts to two branches, 180 degrees out of phase. Two impedance matching networks are used to match the source and load on resonance.

Estimates for the parasitics of each segment are in appendix C. We now look into the functionality the capacitive dividers and the bias-tees.

### Capacitive voltage dividers

Each branch, RF+ and RF-, has a capacitive voltage divider which can be used to pick-off a small part of the signal which is then rectified and used to debug the resonator as well as providing the possibility to use active stabilization of the RF voltage amplitude [24]. In the previous design these were separate and not on the PCB [11]. The voltage pick-off is

$$V_{capdiv} = \frac{C_{cdiv,1}}{C_{cdiv,1} + C_{cdiv,2}} V_{in}$$

The values for these capacitors is set to  $C_{cdiv,1} = 1$  pF and  $C_{cdiv,2} = 100$  pF.

### DC Bias port

In total the PCB has five input ports, four of which are DC bias ports. Each DC bias port is connected to one RF electrode and can be used for applying a constant voltage to adjust for static electric fields in the trap. This can take over the functionality of shim electrodes, i.e. there is no need for additional electrodes on the trap and connections to the outside. It can also be used to apply an oscillating electric field on resonance with

#### 4. Two-phase resonator PCB

the motional frequency of the ion, exciting the secular motion. Finally, it is used for ion crystal reordering sequences. Placed after the DC bias port is a first order low pass RC filter with a cut-off of

$$f_{-3dB} = \frac{1}{2\pi RC} = \frac{1}{2\pi 100\text{k}\Omega \cdot 1000\text{pF}} \approx 1.6\text{kHz}.$$

The reordering sequence for the mixed species ion crystal, where a time-dependent voltage is applied on the RF electrodes, sets a lower bound on this cut-off frequency. Although the cut-off is substantially lower than the motional trap frequencies if single  $\text{Be}^+$ ,  $f_{x,y,z} \approx 1 - 2 \text{ MHz}$ , exciting the motion of the ion is still possible.

#### Tuning the matching network

To tune the matching network, such that the  $50\Omega$  source and the load are matched on the resonance frequency, we need a value for the load,  $Z_L$ . To do so we remove the matching networks from the model, run the simulations and calculate the load on resonance.

The matching network is robust against tolerances in the values of the matching components,  $C_M$  and  $L_M$ . This means that if we are constrained by e.g. range of available coils and capacitors we can still achieve good matching and hence voltage amplification of the resonator. The values of the matching components are set to  $C_M = 1000\text{pF}$  and  $L_M = 10\text{nH}$ . If  $C_M$  changes up to  $\pm 10\%$ , with  $L_M$  fixed, the gain changes by at most by  $0.001\%$  and the resonance frequency at most by  $0.2\text{MHz}$ . Similarly, if  $L_M$  changes up to  $\pm 10\%$ , with  $C_M$  fixed, the gain changes at most by  $0.007\%$  and the resonance frequency at most by  $0.3\text{MHz}$ .

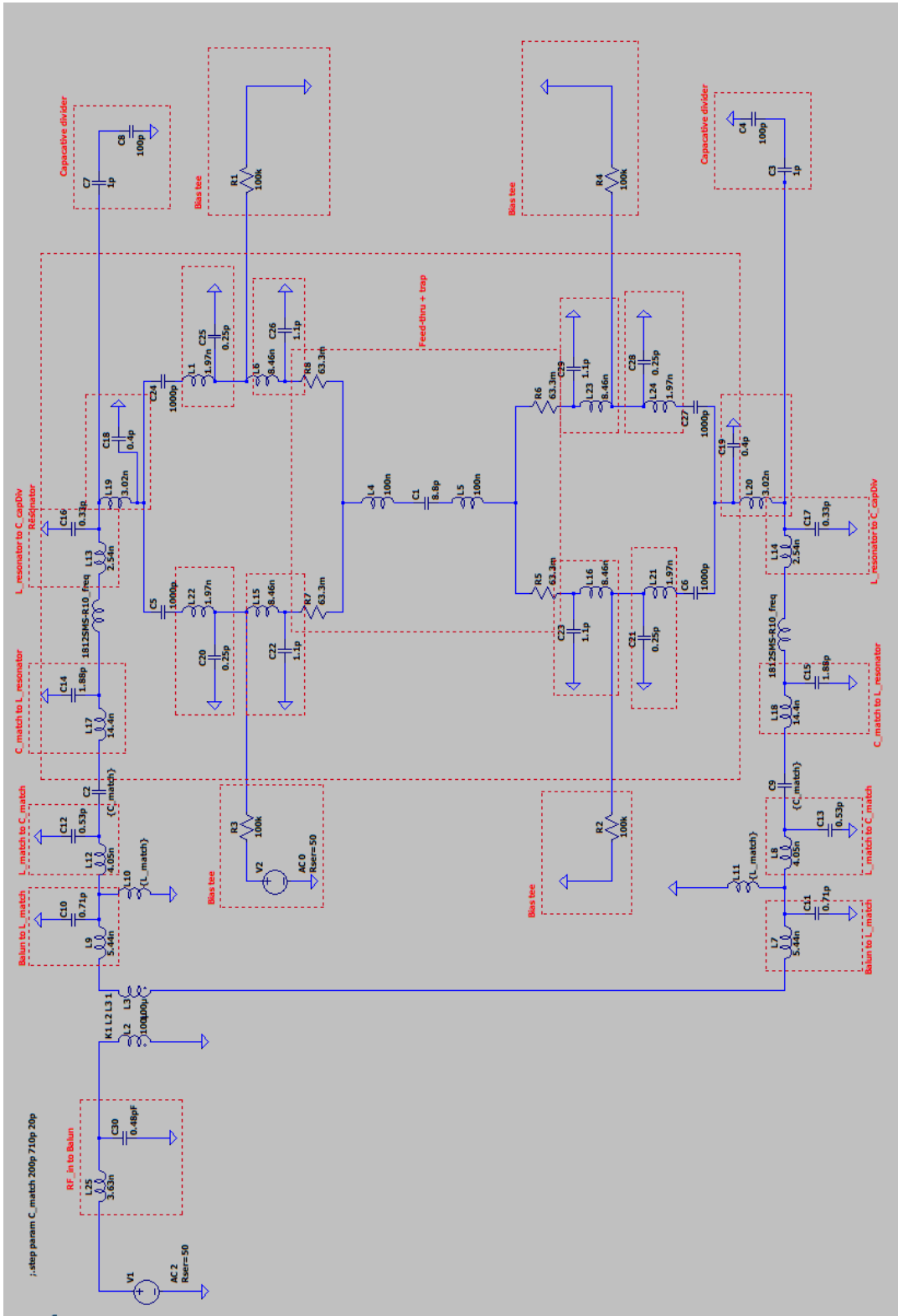


Figure 4.2.: LTspice model of the trap circuit including all components and PCB parasitics. All trace parasitics are modelled as lumped model transmission lines [21, 23].

## 4. Two-phase resonator PCB

### 4.3. Assembling the new Resonator PCB

The fully assembled PCB is seen in figure 4.3. For a full list of components and a layout schematic see Appendix C. There are seven SMA ports on the front, one RF input, four bias-tee ports and two pick-offs to probe the voltage of both branches, RF+ and RF-. On the back there are four pins, one for each electrode, which connect to the feed-through. There is a dedicated ground connection, which is then connected to the ground of the optical table.

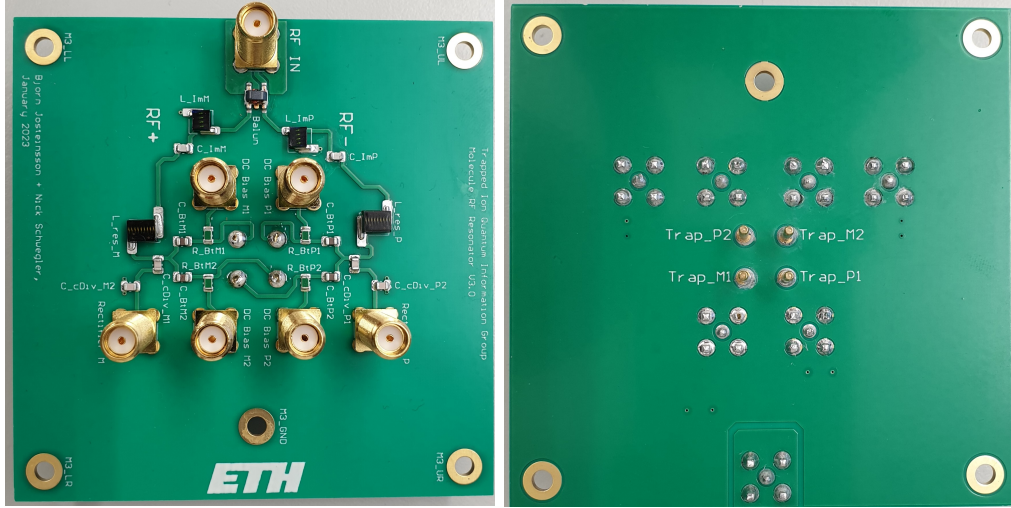


Figure 4.3.: Assembled resonator PCB **Left:** Front side. There are seven SMA connections, one RF input port, four DC bias ports and two pick-offs to measure the voltage for each branch, RF+ and RF-. Each branch has a matching network and a resonator coil. **Right:** Back side. The four pins connect to the feed-through, using barrel connectors, leading to the trap.

#### 4.3.1. Testing and comparing to simulations

The assembled PCB was put in a housing and connected it to the trap. To measure the resonance frequency a FieldFox network analyzer (NA) was used to measure the scattered power,  $S_{11}$ , when connected to the RF input. Measurement of  $S_{11}$  are seen in figure 4.4. Only one resonance is observed at  $\Omega_{RF,0}/2\pi = 78.57$  MHz and the measured quality factor (eq. 2.32) is  $Q = 2 \cdot 78.57/1.9 = 83$ . In simulations the resonance frequency is  $\Omega_{0,sim}/2\pi = 76.1$  MHz. This mismatch is explained by the fact that only estimates were used for component values in simulations. Better estimates would have been possible by removing the previous resonator and performing individual measurements on the trap and chamber.

Another important feature of the new resonator is the filtering provided by the second order high-pass up-converting matching network. Previous resonator showed a small

### 4.3. Assembling the new Resonator PCB

resonance close to the motional trap frequencies [11]. From the frequency sweep in figure 4.4, low frequencies are suppressed, with  $S_{11}$  close to 0dB, i.e. almost all the input power is reflected.

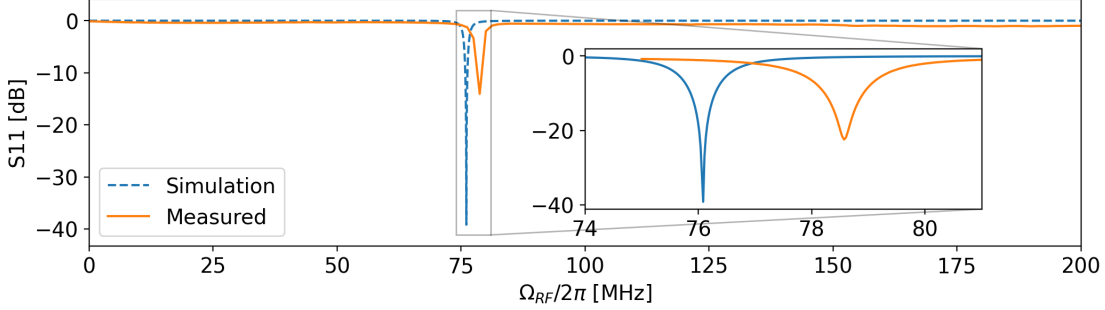


Figure 4.4.: Scattered power,  $S_{11}$ , of the RF input port with the trap connected. The frequency is swept from 30kHz to 200MHz. There is only one resonance in both measurement and simulation. Measured resonance is at  $\Omega_{RF,0}/2\pi = 78.57$  and simulated at  $\Omega_{RF,0,sim}/2\pi = 76.1$  MHz. At frequencies around the motional modes, below 10 MHz, almost all of the power is reflected.

Using the new resonator we managed to trap a single  $\text{Be}^+$  ion. To fine tune the RF drive frequency ion we measure the radial trap frequency for one of the radials, while changing the frequency of the RF source. To measure the radial trap frequency we apply an oscillating electric field to our trap electrodes, which excites the ion motion when resonant with the secular frequency,  $\omega_x$ . This results in a drop in fluorescence due to Doppler shifts [8]. At resonance,  $\Omega_{RF,0}$ , the radial trap frequency is maximized because the secular frequency is proportional to the voltage on the RF electrodes,  $\omega_x \propto U_{RF}$  (eq. 2.11). From this measurement, in figure 4.5, the resonance sits at  $\Omega_0/2\pi = 78.71$  MHz. From trap simulations, for given secular frequencies and drive frequency, we determine the voltage at the trap, 103.4 V<sub>pp</sub>. Then, using the input voltage at of 12.6V the voltage gain is  $G_{V_{v3}} = 8.2$ . This is improved compared to previous generations of molecule resonators,  $G_{V_{v2}} = 4.7$ [11] and  $G_{V_{v1}} = 6.3$ [22].

Adjusting the inductance of the feed-through from 100nH to 50nH and the trap capacitance from 8.8pF to 10.18pF the simulated resonance is at the same frequency as the measured value and the simulated voltage gain is,  $G_{V,sim} = 10.5$ .

The resonance frequency of the new resonator is close to the frequency that some acousto-optic modulators (AOM) operate at, 80 MHz. Some RF signal might therefore leak into the resonator. The opposite might also be problematic, where the trap RF circuitry might affect the AOM's. When measuring the reflected signal from the resonator with a NA this 80 MHz component was observed. However, this might also have been a pick-up of the 80MHz signal from the SMA cable connected to the NA. During testing and initial use of the resonator there were no signs of this having an effect on the ion or the lasers.

The final test with the new resonator was to investigate the DC bias ports. We

#### 4. Two-phase resonator PCB

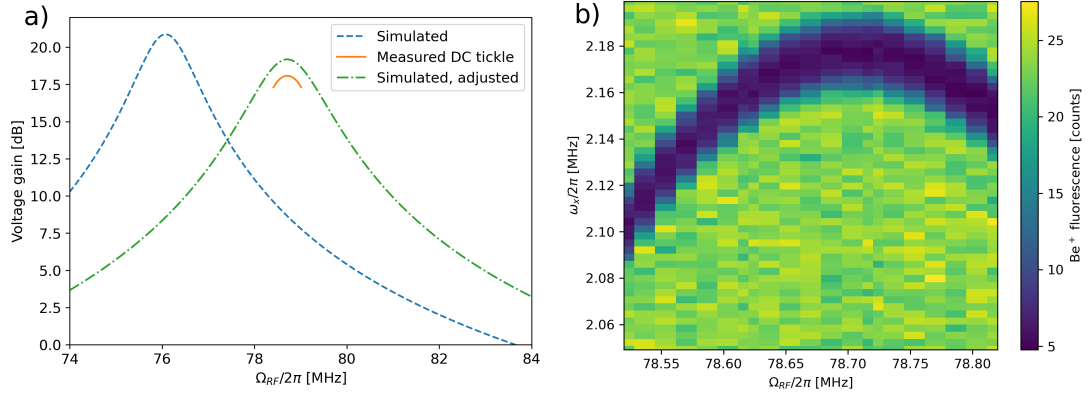


Figure 4.5.: **a)** Voltage amplification on the trap electrodes. Two curves show the simulated value with initial and adjusted values. The small curve is the measured gain from the measurement in b). **b)** Exciting the motion of the x-radial, which leads to a drop in fluorescence due to a Doppler shift, while changing the frequency of the RF source. At resonance,  $\Omega_{RF,0}$  the trap frequency,  $\omega_x$  is maximized.

therefore measure the scattered power,  $S_{11}$ , from all four DC bias ports. The lowest frequency attainable with the NA is 30kHz, above which we observed that almost all of the signal is reflected. This was as expected, as the RC-filter has a cut-off of  $f_{-3dB} \approx 1.6$  kHz. This means strong suppression of noise at high frequencies. Nevertheless, these ports can still be used for exciting the secular motion of the ion, up to a few MHz.

#### 4.3.2. New RF amplifier

The increased voltage gain of the new resonator gave the possibility to use a new RF amplifier while still achieving the desired radial secular frequencies. The new amplifier has lower maximum output power but also substantially lower noise figure (NF). A summary for the new and old RF amplifiers is seen in table 4.1.

Amplifier	Gain (dB)	NF (dB)	1dB point (dB)
Mini-Circuits PHA-13HLN+	24.3 (@20MHz)	1.2 (@20MHz)	27.3 (@20MHz)
Mini-Circuits TIA-1000-4	23.15 (@100MHz)	13.27 (@100MHz)	40.63 (@100MHz)

Table 4.1.: Specifications of the old RF amplifier (Mini-Circuits TIA-1000-4) and the new RF amplifier (Mini-Circuits PHA-13HLN+).

To test the new amplifier we measure the power before and after the amplifier, while changing the power of the RF source. From this the gain curve, seen in figure 4.6, is extracted. The max output is 26.8 dBm or 13.8  $V_{pp}$ . For certain radial trap frequencies we need a certain voltage on the trap RF electrodes. Having  $\approx 13 V_{pp}$  at the input of the new resonator ( $\approx 103 V_{pp}$  on the electrodes) is sufficient to reach the previous trap

### 4.3. Assembling the new Resonator PCB

frequencies,  $\{\omega_x, \omega_y, \omega_z\} = 2\pi \times \{2.1, 1.9, 1.1\}$  MHz. However, the headroom is small and the amplifier is operated at a point where compression becomes noticeable, which can lead to higher order harmonics and inter-modulation. During initial testing this showed no adverse effects. In figure 4.6 we also see the voltage at the RF+ pick-off measured using a rectifier [11] and a multi-meter.

We expect the improved gain allowing for a better RF amplifier to lead to better motional coherence and heating rates for the radials. However, this is yet to be measured.

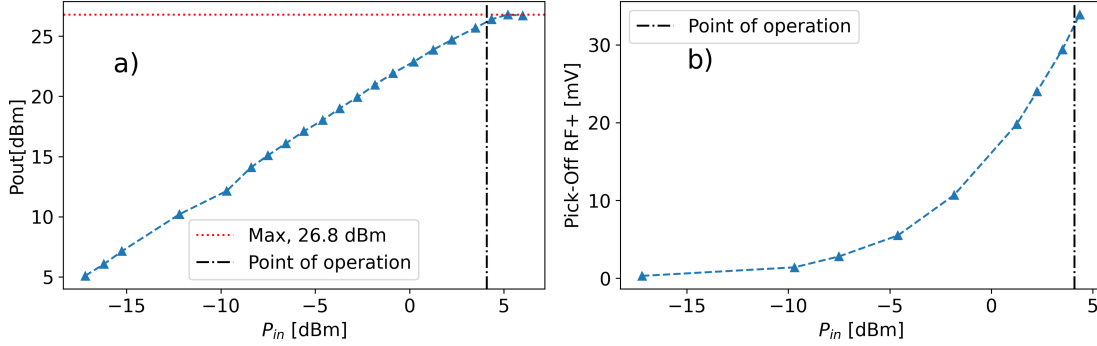


Figure 4.6.: New RF amplifier. Vertical lines mark operating point to reach trap frequencies of,  $\{\omega_x, \omega_y, \omega_z\} = 2\pi \times \{2.1, 1.9, 1.1\}$  MHz. **a)** Gain curve of the amplifier, maxing out at 26.8 dBm, sufficient to reach desired trap frequencies. **b)** Voltage measured using a rectifier [11] connected to the pick-off of the RF+ branch.



# Micromotion measurements

---

In chapter 2 we saw methods to measure MM. In particular the ratio between the Rabi rate of the MM sideband and carrier can be used to determine the modulation index. In this chapter we investigate MM using the sideband method by adding a new beam-line, which couples to all motional modes.

## 5.1. Beam-lines

For the sideband method, using Raman transitions, we need a pair of Raman beams. By choosing the beam geometry, we can couple to different motional modes. In figure 5.1 we see the relevant beam-lines for driving Raman transitions in single Be with a wavelength of 313nm, as well as their direction with respect to the motional normal modes. Previously, there was only one set of Raman beams,  $R_{90}$  and  $R_{co}$ , which couples to the axial mode. For this project an extra beam-line was added by splitting up the  $R_{co}$  and reaching the trap from the bottom. This gives another set,  $R_{bottom}$  and  $R_{90}$ , which couples to all motional modes.

In order to be able to drive the MM sideband, which has a frequency offset of 60 – 80MHz from the carrier, we replaced a single pass AOM with double pass 200MHz AOM. With the new double pass AOM we reach a detuning of +80 MHz from the carrier with high diffraction efficiency.

To be able to fully quantify and see MM in three dimensions a third set of Raman beams is necessary. This was not implemented for this thesis. For future reference, we refer to this possible extra beam as  $R_{counter}$  as it would counter-propagate to the  $R_{co}$ . In table 5.1 we see the L-D parameters for each combination of beams as well as their normalized directions where x,y are the direction of the radial normal modes and z the axial.

## 5.2. Measuring MM using stimulated Raman transitions

In this work we focused on measuring MM with one set of beams,  $R_{bottom}$  and  $R_{90}$  as the other available combination only probes the axial direction, where we expect the MM to be small.

When we scan the detuning of the Raman beams, seen in figure 5.2, we can observe a carrier transition at zero detuning, but also multiple sidebands e.g. see blue and red sidebands for all three motional modes. We also see the second order axial sideband and

## 5. Micromotion measurements

Raman pair	$\eta_x$	$\eta_y$	$\eta_z$	$\Delta\vec{k}/ \Delta\vec{k} $
$R_{90}$ & $R_{bottom}$	0.07	0.40	0.32	$\{0.1464, -0.8535, 0.5\}$
$R_{90}$ & $R_{co}$	0	0	0.635	$\{0, 0, 1\}$
$R_{co}$ & $R_{counter}^i$	0.162	0.169	0.318	$\{-0.5, -0.5, -0.7071\}$

Table 5.1.: Lamb-Dicke parameters for different beam combinations assuming the following trap frequencies for single a  $\text{Be}^+$ ,  $\omega_x/2\pi = 2.15$  MHz,  $\omega_y/2\pi = 1.98$  MHz and  $\omega_z/2\pi = 1.12$  MHz.  $\Delta\vec{k}$  is in the coordinate system of the motional normal modes.

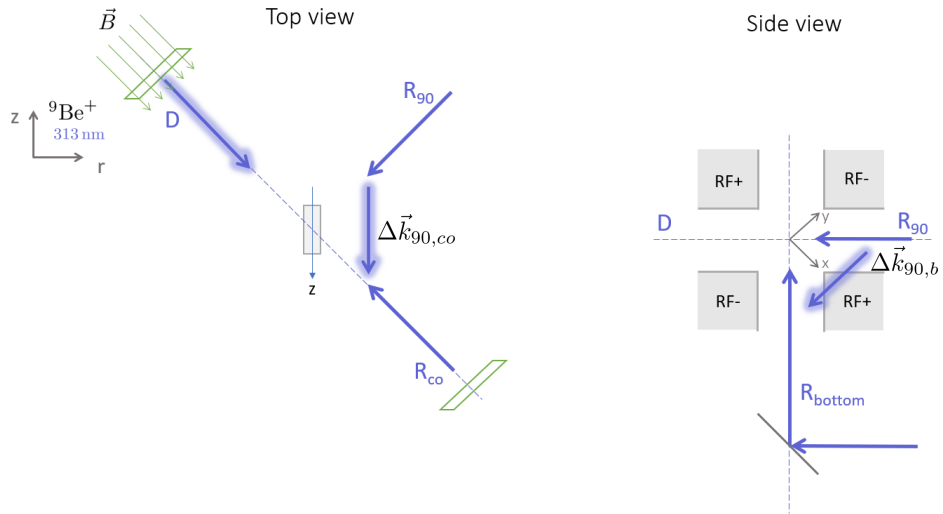


Figure 5.1.: Beam-lines in the molecule setup and how they enter the trap. X- and y-coordinates are the radial normal modes and z is the axial normal mode. There are three beams which can be used to address two different Raman transitions,  $R_{90}$  &  $R_{co}$ , which couples to axial mode only, and  $R_{90}$  &  $R_{bottom}$ , which couples to all modes. Credit: Nick Schwegler

other intercombination terms. This is because the set  $R_{bottom}$  and  $R_{90}$  couples to all motional modes and has high L-D parameters, i.e. couples strongly to the motion.

Also seen in figure 5.2 is a frequency sweep around the MM sideband at  $\Omega_{RF}/2\pi = 67.5$  MHz. There we also see motional sidebands and other inter-combinations around the MM sideband.

For comparison we calculate the spectrum numerically by solving the ion EOM, eq. 2.4. An example of the trajectory along the x-radial for two different displacements is seen in figure 5.3. The initial amplitude of the secular motion is the same but we observe that when the ion is displaced more MM is induced. Using the trajectory we calculate

## 5.2. Measuring MM using stimulated Raman transitions

the electric field, eq. 2.25. In figure 5.2 we see the simulated spectrum both around the carrier and the MM sideband, with the peaks corresponding to the measured spectrum.

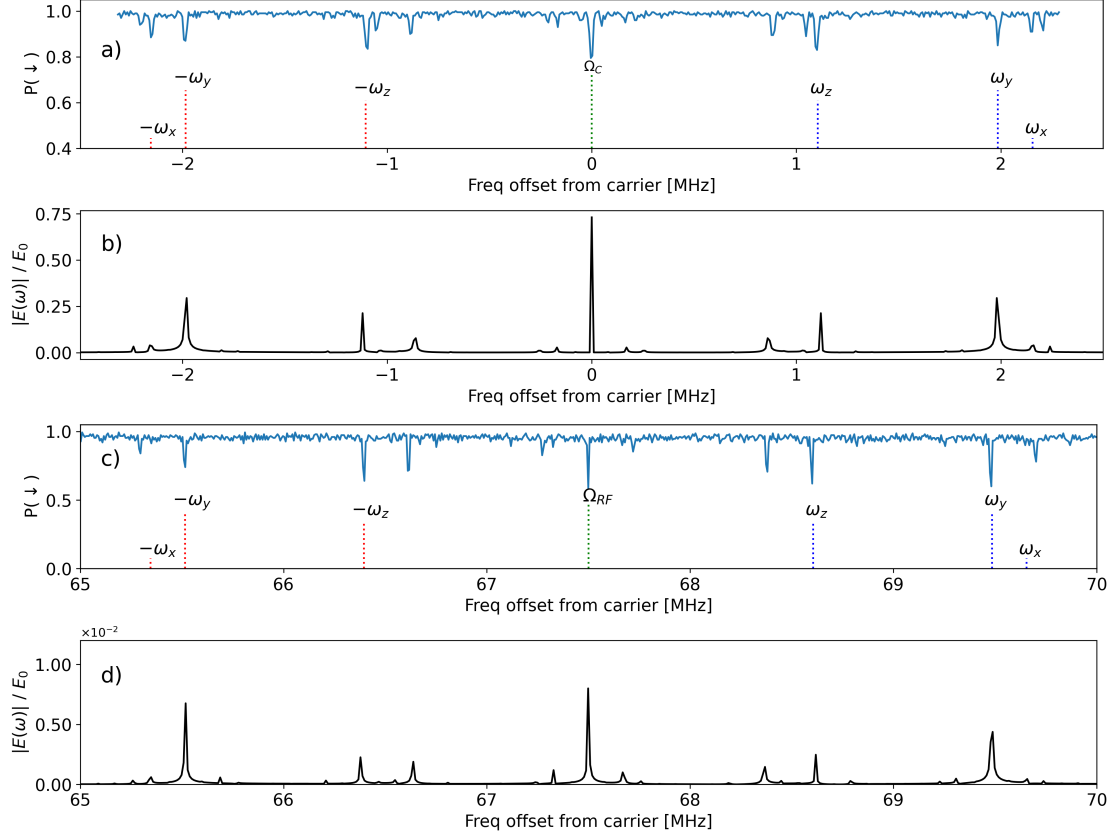


Figure 5.2.: Driving stimulated Raman transitions with the set of beams,  $R_{90}$  and  $R_{bottom}$ . **a)** Sweeping the frequency around the carrier with. The beams couples to all motional modes and peaks are observed at zero detuning (carrier) as well as at red and blue first order sidebands and for other higher order intercombinations. The first order sidebands are marked, where the peak height corresponds to the L-D parameter for each mode. **b)** Simulated spectrum using the solution to the ion EOM and calculating the electric field in the rest frame of the ion. Peaks at same frequencies as for the measurement in a) are observed. **c)** Sweep around the MM sideband were no MM compensation was made prior to measurement. Same combination of motional modes and inter-combinations as for the carrier sweep are observed. **d)** Simulated spectrum around the MM sideband using the solution to the ion EOM and calculating the electric field in the rest frame of the ion. Peaks at same frequencies as for the measurement in c) are observed.

## 5. Micromotion measurements

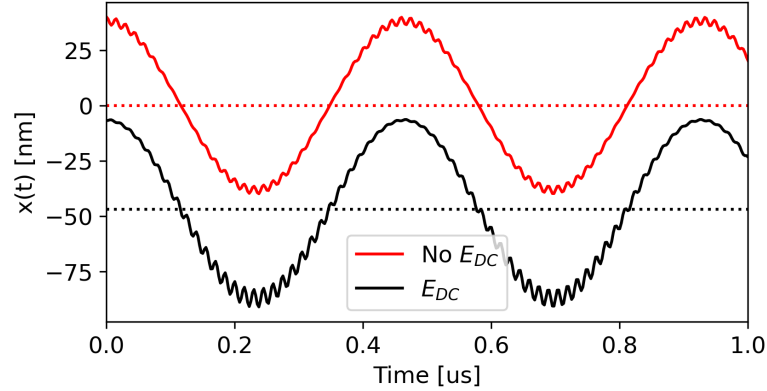


Figure 5.3.: Solving the EOM (eq. 2.4) numerically for both zero and non-zero static electric displacement field,  $E_{DC}$ . The average offset is 0nm and 48nm respectively. In both cases the initial amplitude is  $x_0 = 40\text{nm}$ . As the ion is displaced it experiences more MM.

### 5.2.1. Displacing the ion

When the ion is displaced radially MM increases and hence the measured modulation index,  $\beta$ . In figure 5.4 is a 2D scan where the ion is displaced in both radial directions, x- and y. For the measurement the MM sideband is driven for a fixed time and the probability of the qubit being in a spin down state,  $P(\downarrow)$ , measured. This doesn't yield the modulation index but we see the same qualitative features when comparing to simulations. Firstly, as the ion is displaced further the MM sideband flops faster (lower  $P(\downarrow)$ ) and the modulation index becomes larger. The second feature is that there is a line which is orthogonal to the  $\Delta\vec{k}$  vector of the two Raman beams. Along this line the measurement is insensitive to MM, i.e. the MM is perpendicular to the k-vector of the beam and does therefore not modulate the phase of the laser. The slope of the line is the ratio of the x- and y-coordinates of the  $\Delta\vec{k}$  vector. Also, as the L-D parameter is higher for the y-radial, the modulation index when displacing in that direction is higher compared to the same displacement along the x-radial.

### 5.2.2. Extracting the modulation index, $\beta$

To extract the modulation index,  $\beta$ , we follow the theory in section 2.2, measure the Rabi rate for the carrier and the MM sideband and then extract the modulation index using 2.20. For this we first sweep the frequency of the carrier, sit at the resonance and then flop the carrier. The same is then done for the MM sideband. This is necessary because as the ion moves through the beam it experiences different Stark shifts and therefore a different carrier frequency for each point.

To extract the Rabi rate, a fit of both time traces is made according to a heuristic model

## 5.2. Measuring MM using stimulated Raman transitions

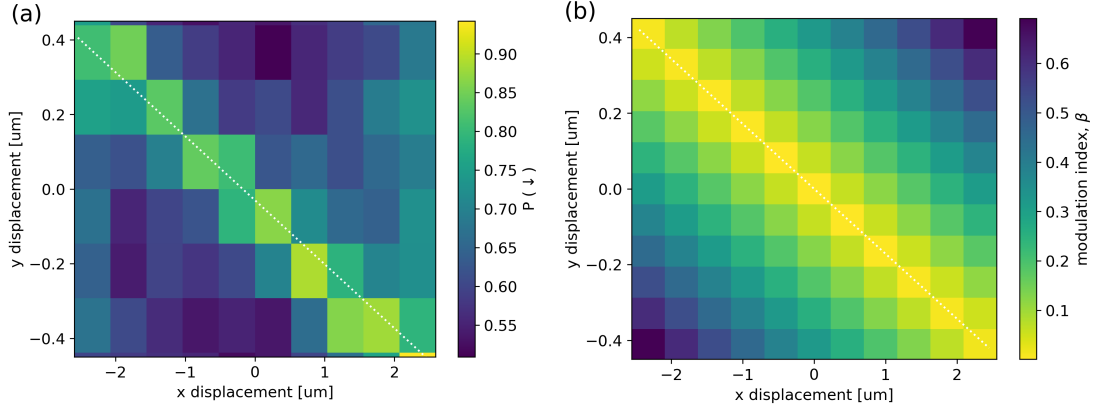


Figure 5.4.: Displacement a long radial x and y direction. **(a)** Sitting at the MM sideband and driving for a fixed time, measuring the contrast. **(b)** Simulated modulation index,  $\beta$ , by solving the ion classical EOM in 3D (Refer to section!). The white dotted line in both pictures represents the ratio of the x- and y-components of the  $\Delta k$  vector from the Raman beams driving the transitions. In this directions the measurement is not sensitive to MM. This is also why the scaling is different for the axis, x and y.

$$P(\downarrow) = 0.5 + (0.5 - c) \cdot \exp(-(\gamma \cdot t)^2) + c \quad (5.1)$$

with two fit parameters,  $\gamma$ , and  $c$ , where  $c$  is a constant to account for an offset when  $P(\downarrow)$  does not go to 0.5, due to bad frequency calibration. We assume the Rabi rate to be  $\Omega = 1/\gamma$  and the error estimate is extracted from the standard deviation of the fit  $\Delta\Omega = \Delta\lambda/\lambda^2$ . Then  $\Delta\beta = \Delta\Omega_{MM}/\Omega_{carrier} + \Omega_{MM}\Delta\Omega_{carrier}/\Omega_{carrier}^2$ . Examples of carrier and MM sideband time-traces and corresponding fits can be seen in figure 5.5. This heuristic model does correctly capture the Rabi rates for the carrier and MM sideband but we assume that the Rabi rate is proportional to the rate,  $\gamma$ .

We now displace only along the y-radial and measure the modulation index, see figure 5.5. For comparison we plot the simulated modulation index from both the solution of the ion EOM and the finite element simulations<sup>ii</sup>, simulating the residual RF field (see section 2). Both the EOM simulation and the measurement rely on the approximation  $\beta \ll 1$  which becomes worse as the displacement is increased.

The simulated modulation index using the EOM solution is a factor  $\sqrt{2}$  larger than the residual field simulations. When simulating other beam geometries this was also the case. A possible reason is incorrectly scaled vectors for the beam-lines or overlooked factors when calculating the Fourier transform of the electric field.

During measurements drifts in the MM compensation points were observed when repeatedly doing MM compensation. MM compensation is done by displacing the ion in

<sup>ii</sup>Finite element simulations by Nick Schwegler

## 5. Micromotion measurements

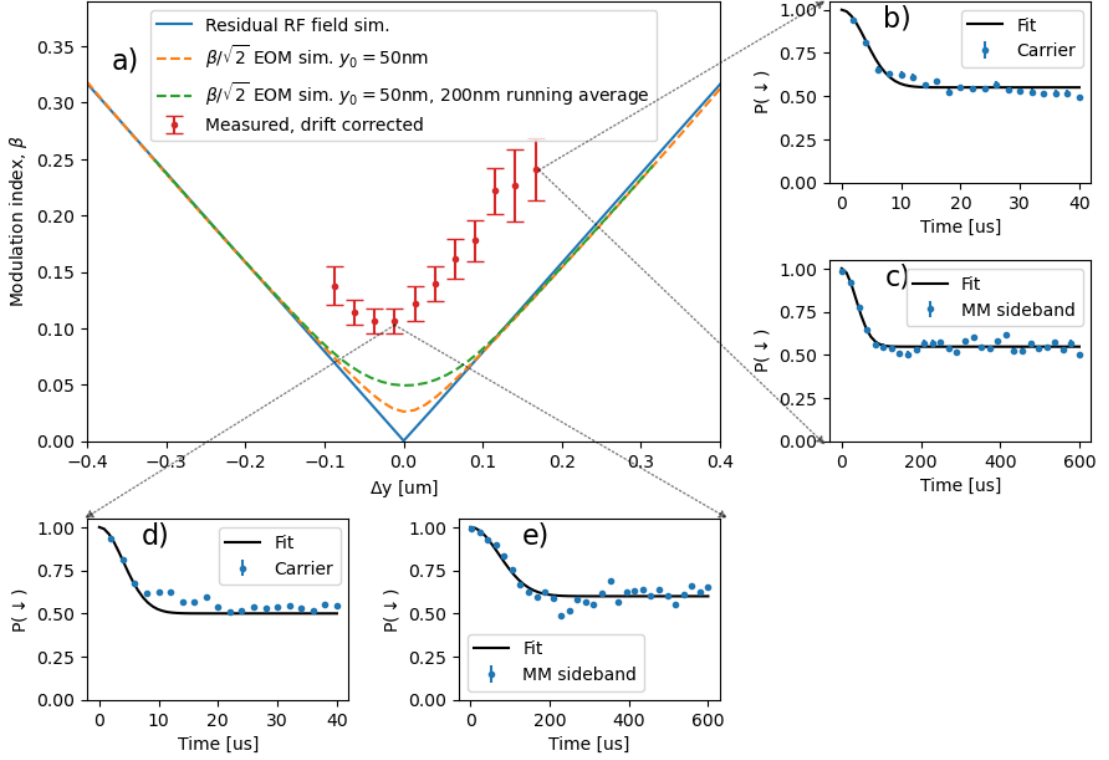


Figure 5.5.: **a)** Measured and simulated modulation index for y-radial displacement. Simulations were made by solving the EOM of motion, eq. (2.4), with initial condition,  $y_0 = 50$  nm, simulating a thermal state. In that case the modulation index does not go to zero. A running average of the thermal state is also taken, corresponding to a displacement due to observed voltage fluctuations on a DAC leading to the RF electrodes. Simulations using the residual RF field, show a modulation index that goes to zero at zero displacement. To extract the modulation index from measurements the flopping rate is determined for the carrier (**b** and **d**) and the MM sideband (**c** and **e**) by fitting a heuristic model, eq. 5.1.

the radial direction and parametrically exciting the motion by modulating the RF signal. Due to Doppler shifts the fluorescence drops when the ion has higher MM. This drift was linear, resulting in a change in MM compensation point of  $\approx 0.08\mu\text{m}$  over 42 minutes. To account for this, the position for each point has been corrected using a linear fit to the drift. Thus, the point distribution is skewed to positive values of displacement.

This drift might originate from static charges on the trap, high impedance shorts and/or a DAC which provides voltage for the end-cap electrodes. We can exclude the DAC providing voltage to the DC bias of the RF electrodes because we measured the applied voltage, as seen in figure 5.6. The output fluctuates but there is no evident drift over 30 minutes.

## 5.2. Measuring MM using stimulated Raman transitions

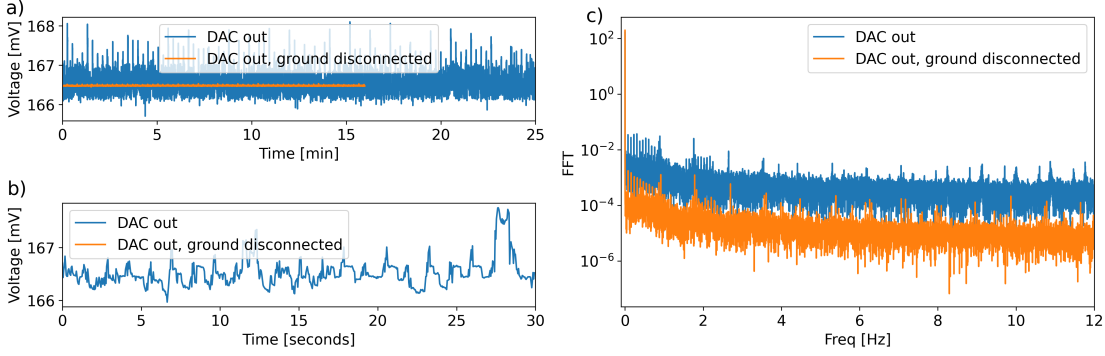


Figure 5.6.: **a)** Voltage output for one of the DACs connected to DC bias tee leading to the trap RF electrodes. Measurements over  $\sim 30$  minutes with the trap ground connected and disconnected, measured using a Keithley DMM6500. **b)** Same measurement as in a) but for a time interval which is approximately the time it takes to measure the carrier and MM sideband for each position ( $\sim 30$  seconds). **c)** Fourier transform of both traces in a). The noise floor is much lower when the trap ground is disconnected but the same periodic features are observed.

The modulation index does not vanish at the MM compensated point, which can have different explanations. First, due to imperfections in the trap geometry there is some residual RF field. Second, there could be a phase mismatch on electrodes, although previous measurements [11] and circuit simulations (see chapter 3) suggest this is negligible. Third, the ion is hot, in a thermal state where it explores large enough region such that there is always some MM visible, which was likely the case for these measurements, as only Doppler cooling was used. Assuming that we reach the Doppler temperature, eq. 2.22, using a dipole transition with a natural linewidth of  $\Gamma = 2\pi \cdot 20$  MHz [25], gives a mean phonon number of  $\bar{n} \approx 4.5$  for the y-radial ( $\omega_y/2\pi = 1.98$  MHz). A thermal state with this phonon number has a Gaussian wavepacket and the RMS width of the wavepacket is, according to eq. 2.23,  $\Delta y \approx 50$  nm. This means even when ion sits at a position with minimal MM it still explores regions with higher MM, yielding a non-zero modulation index. If we assume a thermal state and calculate the upper bound for the ratio of MM sideband to carrier according to eq. 2.24 we find a modulation index of  $\beta_{thermal,bound} = 0.076$ .

Another reason which can lead to a non-zero modulation index at optimal ion position are voltage fluctuations on the RF electrodes. We observe fluctuations when probing the output signal of a DAC, as seen in figure 5.6. The output of the DAC is connected to the bias-tees leading to the RF electrodes. The measurement of carrier and MM sideband time traces take  $\sim 30$  seconds. For a time trace of 30 seconds the DAC voltage has jumps of up to 1mV. This is also observed when probing the feed-through, where the signal from the DAC has been low-pass filtered. For the y-radial, 1mV change in the DAC voltage equals a displacement of,  $\Delta y \approx 0.2$   $\mu\text{m}$ , meaning the ion moves considerably during the

## 5. Micromotion measurements

measurement, yielding a higher modulation index.

When comparing the measured modulation index to simulations we see an offset, but the slope of the curve is similar to simulations. The offset is likely due to the heuristic model used to extract the modulation index. The model fails to catch some features of the curves. Firstly, the MM sideband exhibits damped oscillations that lead to the fit favoring faster Rabi rates. For the carrier, the fit catches the initial decay but between 10-20 us we notice a feature which it does not catch. Attempts to fit the time evolution using the full expansion for the Rabi rate [14] assuming a thermal state for ion did not work for the MM sideband. Further analysis and a better model is needed. Another possibility is to cool all the three modes further, ideally to the ground state, would simplify the analysis and could improve the measured modulation index. Ultimately, the combination of the ion being in a thermal state, the voltage fluctuations and drifts limit the precision of the measurement. To be able to measure the intrinsic MM these limitations need to be overcome.

### 5.2.3. Comparing the sideband and time-tagging method

The smallest modulation index measured here,  $\beta = 0.11 \pm 0.01$ , is higher than what was observed before using a photon time-tagging method where  $\beta = (0.49 \pm 1) \times 10^{-3}$  [11]. This was measured using the detection beam which has different coupling to motional modes compared to Raman beams used for the measurement in this thesis, and can therefore not be directly compared. In both cases the ion was in a thermal state. The difference is that the sideband method is sensitive to the thermal motion where as the time-tagging method is not sensitive to the motion state of the ion [17], possibly explaining the large discrepancy. As explained in chapter 2 that if the wavepacket of the ion extends into regions with MM, the sideband method yields a higher modulation index. However, using time-tagging method, given the ion has a symmetric wave packet and sits at position with minimal MM, it is equally likely to explore regions that have the opposite phase when measured. This leads to the total effect cancelling out as illustrated in figure 5.7.

Finally we comment on the correction factor,  $\alpha$ , in eq. 2.18 and calculate it from eq. 2.14. Using the electric field value at the trap center arising from finite element simulations we find  $\alpha = 0.35$  for both radial, x- and y, directions. In previous work [11] the assumption was  $\alpha = 1$ . This alone does however not explain why the observed phase mismatch was much smaller than anticipated.

## 5.2. Measuring MM using stimulated Raman transitions

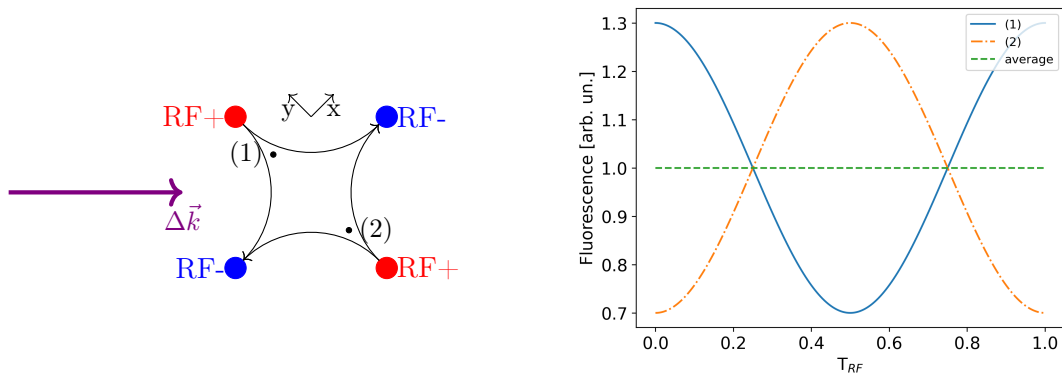


Figure 5.7.: The phase of the time-tagging signal flips when the crosses the point with minimal MM. If the ion is in a thermal state the wavepacket is symmetric and the ion is equally likely to explore regions (1) and (2). As the time-tagging method averages the signal over many RF cycles the effect cancels out and the measured modulation index is low.



## Conclusion and outlook

---

In this thesis a circuit model was developed to investigate phase shifts induced on electrodes due to trap wiring asymmetry. Simulations using this model showed the induced phase shift was smaller than anticipated. Based on this insight a new iteration of a PCB resonator was developed. Finally, micromotion was investigated by driving the carrier and MM sideband using stimulated Raman transitions.

The single-phase trap RF drive circuit model developed for the linear Paul trap in this thesis is composed of several components. The trap is modelled as capacitors and a PCB, which sits in vacuum and connects a feed-through to the trap, is also modelled as capacitors. The feed-through, which are long metallic rods, are modelled as inductors. The final part of the model is the resonator PCB which houses the resonator coil and the matching network. The circuit simulation results revealed that the induced phase shift between electrodes is smaller than anticipated, but also identified scenarios which should be avoided when designing a linear Paul trap. Specifically, asymmetries in the wiring close to the trap, especially capacitive, should be avoided. This can happen if the wiring for one of the electrodes passes close to a ground plane which induces parasitic capacitance.

The new version of a PCB resonator using lumped elements develop in this thesis was based on previous designs [11, 22]. The new design omits phase-shifters [11] as the phase shift on electrodes was smaller than anticipated, initially seen in MM measurements using time-tagging [11] and now also in circuit simulations. Upgrades to the resonator were made in order to minimize capacitive load of the PCB and hence maximize the voltage gain at the trap. The measured voltage gain of the new resonator is  $G_V = 8.2$  and the resonance frequency is  $\Omega_{RF,0} = 78.72$  MHz. The new resonator also shows better low frequency suppression around the motional frequencies of the trap, which are below 10 MHz. Increased voltage gain allowed for a new RF amplifier to be used to drive the resonator, which has a much lower noise figure, 1.2dB at 20MHz, than the previous one, 13.27dB at 100MHz. However, the new RF amplifier operates at a point close to where compression becomes noticeable, so it might be beneficial to lower the resonance frequency of the resonator. Lowering the resonance frequency might also be needed, as currently it could interfere with AOMs that operate at 80MHz. This can be achieved easily, due to the modularity of the PCB. The combination of higher voltage gain, higher trap drive frequency and a new RF amplifier are expected to improve motional coherence and heating rates of the radial modes.

A new beam line was added to do MM measurements using the sideband method, where the ratio of Rabi rate of the MM sideband and carrier transition yield the modulation

## 6. Conclusion and outlook

index,  $\beta$ . For the MM measurement the ion was displaced by approximately  $\pm 0.1 \mu\text{m}$  along the y-radial normal mode. A non-zero value for the modulation index was observed at the point with minimal MM, with a value of  $\beta = 0.11 \pm 0.01$ . Using the sideband method, a non-zero value of the modulation index can be expected when the ion is in a thermal state. Another effect observed, which could lead to a higher modulation index around the optimal point, are slow voltage fluctuations on a DAC leading to the RF electrodes, introduced by a ground loop. Fluctuations of up to 1mV were observed. This could result in a displacement of the ion of almost  $0.2 \mu\text{m}$ , meaning the ion moves around during the measurement and hence explores regions with increased MM. Further analysis is needed to confirm whether this is the case and what the source of the proposed ground loop is. A constant linear drift, in MM compensated point, was observed over a few hours. This drift was on the order of  $0.1 \mu\text{m}$  per hour. This drift is possibly due to electric patch potentials on the trap generated by UV lasers, high impedance shorts or drifts in a DAC which supplies voltage to the end-cap electrodes of the trap. Finally, the heuristic model utilized to analyze the time traces generated by driving the carrier and MM sideband failed to accurately represent the phenomenon of the flopping. This is likely the reason why a constant offset is seen when comparing to simulations. A better understanding and a better model is needed to fit the time trace, especially when driving the MM sideband. Another solution is to ground state cool all three motional modes before repeating the measurements. Cooling to the ground state is also needed to find a lower bound to the intrinsic micromotion, as the sideband methods is limited by the thermal motion of an ion cooled to the Doppler limit. To then fully characterize the MM amplitude in three dimensions another beam-line is needed.

# Bibliography

1. Bruzewicz, C. D., Chiaverini, J., McConnell, R. & Sage, J. M. Trapped-ion quantum computing: Progress and challenges. *Applied Physics Reviews* **6**, 021314. eprint: <https://doi.org/10.1063/1.5088164>. <https://doi.org/10.1063/1.5088164> (2019).
2. Brewer, S. M. *et al.*  $^{27}\text{Al}^+$  Quantum-Logic Clock with a Systematic Uncertainty below  $10^{-18}$ . *Phys. Rev. Lett.* **123**, 033201. <https://link.aps.org/doi/10.1103/PhysRevLett.123.033201> (3 July 2019).
3. Chou, C. W., Hume, D. B., Koelemeij, J. C. J., Wineland, D. J. & Rosenband, T. Frequency Comparison of Two High-Accuracy  $\text{Al}^+$  Optical Clocks. *Phys. Rev. Lett.* **104**, 070802. <https://link.aps.org/doi/10.1103/PhysRevLett.104.070802> (7 Feb. 2010).
4. Wolf, F. *et al.* Non-destructive state detection for quantum logic spectroscopy of molecular ions. *Nature* **530**, 457–460. ISSN: 1476-4687. <https://doi.org/10.1038/nature16513> (Feb. 2016).
5. Kienzler, D. *et al.* Quantum Logic Spectroscopy with Ions in Thermal Motion. *Phys. Rev. X* **10**, 021012. <https://link.aps.org/doi/10.1103/PhysRevX.10.021012> (2 Apr. 2020).
6. Home, J. P. Chapter 4 - Quantum Science and Metrology with Mixed-Species Ion Chains. *Advances In Atomic, Molecular, and Optical Physics* **62** (eds Arimondo, E., Berman, P. R. & Lin, C. C.) 231–277. ISSN: 1049-250X. <https://www.sciencedirect.com/science/article/pii/B9780124080904000049> (2013).
7. Micke, P. *et al.* Coherent laser spectroscopy of highly charged ions using quantum logic. *Nature* **578**, 60–65. ISSN: 1476-4687. <https://doi.org/10.1038/s41586-020-1959-8> (Feb. 2020).
8. Schwegler, N. *et al.* *Trapping and ground-state cooling of  $\text{H}_2^+$*  2022. arXiv: 2212.06456 [physics.atom-ph].
9. Paul, W. Electromagnetic traps for charged and neutral particles. *Rev. Mod. Phys.* **62**, 531–540. <https://link.aps.org/doi/10.1103/RevModPhys.62.531> (3 July 1990).
10. Berkeland, D. J., Miller, J. D., Bergquist, J. C., Itano, W. M. & Wineland, D. J. Minimization of ion micromotion in a Paul trap. *Journal of Applied Physics* **83**, 5025–5033. <https://doi.org/10.1063/1.367318> (1998).
11. Edqvist, E. *Characterization of micromotion induced by RF phase shift with photon correlation detection in a Paul trap*. MA thesis (ETH Zurich/KTH, 2022).

## Bibliography

12. Davide, G. *Compact RF Amplifier for Scalable Ion-Traps* PhD thesis (UNIVERSITA DEGLI STUDI DI TRENTO, UNIVERSITÄT INNSBRUCK, 2011).
13. Kienzler, D. *Trapped-ion physics lecture* June 2021.
14. Leibfried, D., Blatt, R., Monroe, C. & Wineland, D. Quantum dynamics of single trapped ions. *Rev. Mod. Phys.* **75**, 281–324. <https://link.aps.org/doi/10.1103/RevModPhys.75.281> (1 Mar. 2003).
15. Brown, L. S. & Gabrielse, G. Geonium theory: Physics of a single electron or ion in a Penning trap. *Rev. Mod. Phys.* **58**, 233–311. <https://link.aps.org/doi/10.1103/RevModPhys.58.233> (1 Jan. 1986).
16. John Alan, R. *Analysis of periodically time-varying systems* (Springer-Verlag Berlin, 1983).
17. Keller, J., Partner, H. L., Burgermeister, T. & Mehlstäubler, T. E. Precise determination of micromotion for trapped-ion optical clocks. *Journal of Applied Physics* **118**, 104501. <https://doi.org/10.1063/1.4930037> (2015).
18. Stopp, F., Ortiz-Gutiérrez, L., Lehec, H. & Schmidt-Kaler, F. Single ion thermal wave packet analyzed via time-of-flight detection. *New Journal of Physics* **23**, 063002. <https://dx.doi.org/10.1088/1367-2630/abffc0> (June 2021).
19. Feynman, R. P. *Statistical Mechanics - A set of lectures* (CRC Press, 1972).
20. An, D. *et al.* Surface trap with dc-tunable ion-electrode distance. *Review of Scientific Instruments* **89**, 093102. eprint: <https://doi.org/10.1063/1.5046527>. <https://doi.org/10.1063/1.5046527> (2018).
21. Steer, M. *Microwave and RF Design - Transmission Lines* (NC State University, 2019).
22. Thomsen, A. *Design of a two Phase Radio Frequency Drive for Ion Traps using a Lumped Elements Resonator*. Semester thesis (ETH Zurich, 2020).
23. Strangeway, R. A., Holland, S. S. & Richie, J. E. *Electromagnetics and Transmission Lines* (RacademicS Publishing LLC, 2020).
24. Johnson, K. G. *et al.* Active stabilization of ion trap radiofrequency potentials. *Review of Scientific Instruments* **87**, 053110. eprint: <https://doi.org/10.1063/1.4948734>. <https://doi.org/10.1063/1.4948734> (2016).
25. Will, C. *et al.* Sympathetic cooling schemes for separately trapped ions coupled via image currents. *New Journal of Physics* **24**, 033021. <https://dx.doi.org/10.1088/1367-2630/ac55b3> (Mar. 2022).

# Coupled Oscillators

For the interested reader we include the following derivation as it was one hypothesis why an induced phase mismatch was smaller than anticipated [11]. This is the case for two capacitively coupled harmonic LCR oscillator.

Writing down the system equations we can use Kirchoff's voltage law for the three loops in conjunction with Kirchoff's circuit laws. We again assume identical LCR resonators,  $C_1 = C_2 = C$  and  $L_1 = L_2 = L$ , that are capacitively coupled via  $C_C$

We obtain for the first loop:

$$i_1 R + L \frac{di_1}{dt} + \frac{q_1 - q_3}{C} = 0$$

where  $q_1$  is the charge on the resonator capacitor and  $q_3$  on the coupling capacitor.

For the middle loop (Coupling):

$$\frac{q_1 - q_3}{C} + \frac{q_3}{C_c} - \frac{q_2 + q_3}{C} = 0$$

Then for the right loop:

$$i_2 R + L \frac{di_2}{dt} + \frac{q_2 + q_3}{C} = 0$$

We can now use the middle equation to get rid of  $q_3$  and only be left with two coupled differential equations for  $q_1$  and  $q_2$

$$q_3 \left( \frac{1}{C_c} - \frac{2}{C} \right) = \frac{1}{C} (q_2 - q_1)$$

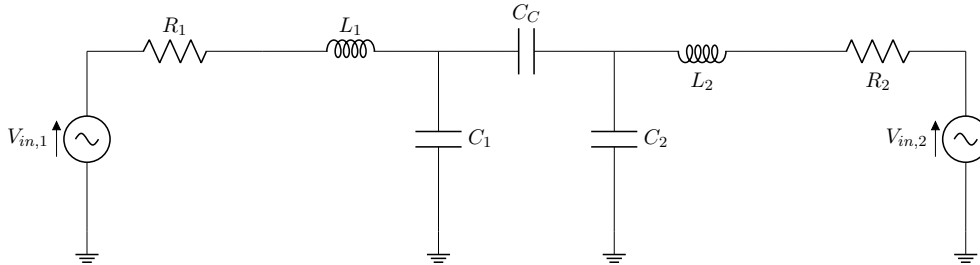


Figure A.1.: Coupled LCR oscillators

### A. Coupled Oscillators

i.e.

$$q_3 = \frac{C_c}{C - 2C_c}(q_2 - q_1)$$

Then using  $i = dq/dt$  our equations become

$$\frac{dq_1}{dt}R + L\frac{d^2q_1}{dt^2} + \frac{q_1}{C} - \frac{C_c}{C - 2C_c}(q_2 - q_1) = 0$$

and

$$\frac{dq_2}{dt}R + L\frac{d^2q_2}{dt^2} + \frac{q_2}{C} + \frac{C_c}{C - 2C_c}(q_2 - q_1) = 0$$

Adding those two together we get

$$\frac{dq_1}{dt}R + \frac{dq_2}{dt}R + L\frac{d^2q_1}{dt^2} + L\frac{d^2q_2}{dt^2} + \frac{q_1}{C} + \frac{q_2}{C} = 0$$

Setting  $q_+ = q_1 + q_2$  this becomes

$$L\frac{d^2q_+}{dt^2} + R\frac{dq_+}{dt} + \frac{q_+}{C} = 0$$

Similarly by subtracting the two equations and setting  $q_- = q_1 - q_2$  we get

$$L\frac{d^2q_-}{dt^2} + R\frac{dq_-}{dt} + \frac{q_-}{C - c_c} = 0$$

We can draw analogy to the case of the mechanical harmonic oscillator, with mass  $m$ , spring constant,  $k$  and damping constant,  $\gamma$ , in which case the equation of motion is:

$$m\ddot{x} + \gamma\dot{x} + kx = 0$$

compared to the LCR resonator

$$L\ddot{q} + R\dot{q} + \frac{q}{C} = 0$$

Now taking the equation for the new normal mode coordinates,  $q_+$  and  $q_-$  and adding the drive to both resonators, assuming they have equal strength,  $V_d$ , but some phase mismatch,  $\phi$ , these equation become:

$$\ddot{q}_+ + (R/L)\dot{q}_+ + \omega_+^2q_+ = (V_d/L)\exp(i\omega_d t) \cdot (1 + \exp(i\phi))$$

$$\ddot{q}_- + (R/L)\dot{q}_- + \omega_-^2q_- = (V_d/L)\exp(i\omega_d t) \cdot (1 - \exp(i\phi))$$

where  $\omega_+^2 = 1/LC$  and  $\omega_-^2 = 1/L(C - C_c)$

To solve these we can make the ansatz,  $q_+ = q_{+0}\exp(i\omega t)$  and  $q_- = q_{-0}\exp(i\omega t)$ .

Before plugging in and solving it is instructive to look at the equations and think about what happens for the cases when  $\phi = 0$  and  $\phi = \pi$ . Intuitively we see the former case only excites the in phase mode and the latter the out of phase mode.

Looking at three different cases,  $\phi = \{0, 180, 165\}$  degrees (figures A.3, A.2, A.4), we can see how we excite different modes and how, if there is a phase mismatch between the two drives the phase synchronizes (figure A.5) when driving on resonance with either mode. We set circuit parameters to  $L = 350\text{nH}$ ,  $C = 8\text{pF}$ ,  $C_C = 4\text{pF}$  and  $R = 1\Omega$ . For this we get resonance frequency for the in-phase,  $q_+$ , mode at  $\omega_+/2\pi = 95.11\text{MHz}$  and the out-of-phase mode at  $\omega_-/2\pi = 67.25\text{MHz}$ .

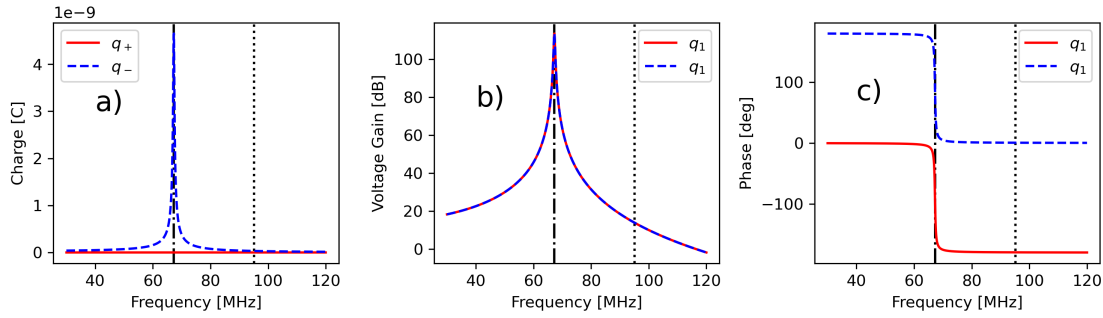


Figure A.2.: The two drives are 180 degrees out of phase, hence only exciting the out-of-phase motion. The phase mismatch is always 180 degrees.

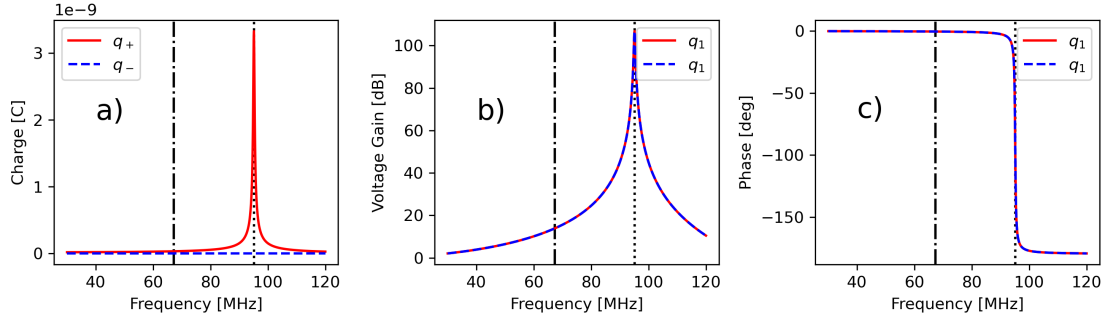


Figure A.3.: The two drives are 0 degrees out of phase, hence only exciting the in-phase motion. The phase mismatch is always 0 degrees.

### A. Coupled Oscillators

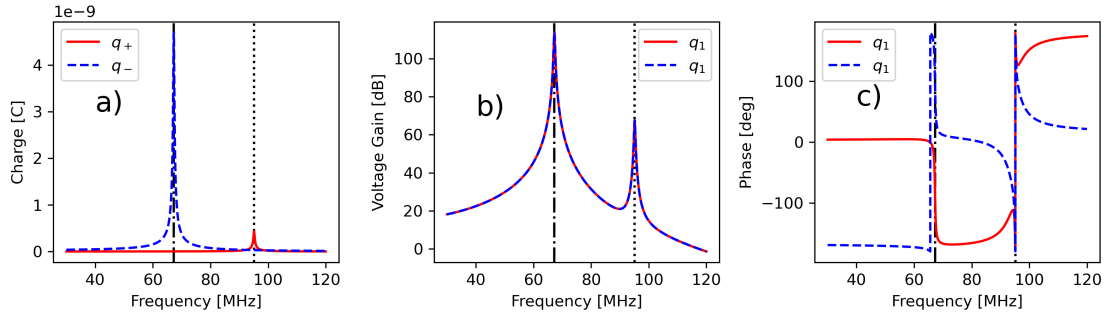


Figure A.4.: The two drives are 165 degrees out of phase, hence exciting both motional modes. When driving on resonance with either motional mode the phase synchronizes.

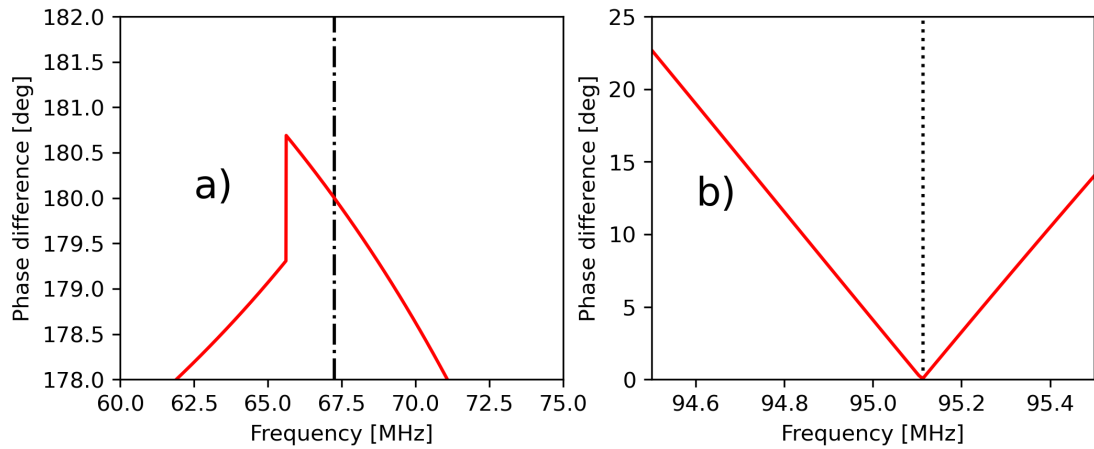


Figure A.5.: Phase difference around the motional modes when the drives are 165 out of phase. At the resonance of either mode **a)** out-of-phase at 67.25 MHz the phase mismatch goes to 180 degrees and **b)** in-phase at 95.11 MHz the phase mismatch goes to 180 or 0 degrees respectively.

# Deriving phase shift on electrodes

The following is a derivation for the phase and voltage mismatch over the capacitors  $C_1$  and  $C_2$  (trap electrodes) in the circuit in figure B.1).

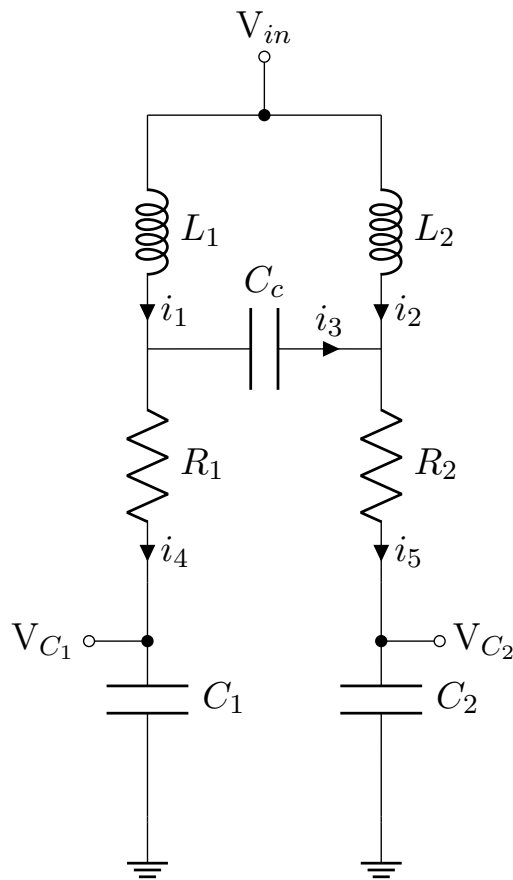


Figure B.1.

If we now denote the left side having the elements  $L_1$ ,  $R_1$  and  $C_1$  and the right with  $L_2$ ,  $R_2$  and  $C_2$  and the coupling capacitor,  $C_c$ . We now have current  $i_1$  through  $L_1$  and  $i_2$  through  $L_2$ . Similarly we have  $i_3$  through  $C_c$ ,  $i_4$  through  $C_1$  and  $i_5$  through  $C_2$ . Then using Kirchoff we can write the following equations:

B. Deriving phase shift on electrodes

$$L_1 \frac{di_1}{dt} + i_4 R_1 + \frac{q_4}{C_1} = L_2 \frac{di_2}{dt} + i_5 R_2 + \frac{q_5}{C_2} \quad (\text{B.1})$$

Using KCL we know  $i_2 = i_3 + i_5$  and  $i_1 = i_4 - i_3$  and KVL gives  $q_3 = C_c \left( \frac{q_5}{C_2} - \frac{q_4}{C_1} \right)$   
This yields

$$L_1 \frac{d^2}{dt^2} \left( q_4 + \frac{C_c}{C_1} q_4 \right) + \frac{q_4}{C_1} + L_2 \frac{d^2}{dt^2} \frac{C_c}{C_1} q_4 + \frac{d}{dt} q_4 R_1 = L_2 \frac{d^2}{dt^2} \left( q_5 + \frac{C_c}{C_2} q_5 \right) + \frac{q_5}{C_2} + L_1 \frac{d^2}{dt^2} \frac{C_c}{C_2} q_5 + \frac{d}{dt} q_5 R_2 \quad (\text{B.2})$$

Now we are interested in the charge on the capacitors  $C_1$  and  $C_2$  because that gives us the voltage on the electrodes. We know assume an ansatz  $q_4 = a \cdot \exp(i\omega t)$  and  $q_5 = b \cdot \exp(i\omega t + \phi)$  where  $\phi$  is an offset between the two branches.

Then plugging in

$$\begin{aligned} a \cdot \exp(i\omega t) [L_1(-\omega^2) \left( 1 + \frac{C_c}{C_1} \right) + \frac{1}{C_1} + L_2 \frac{C_c}{C_1}(-\omega^2) + i\omega R_1] \\ = b \cdot \exp(i\omega t) \exp(i\phi t) [L_2(-\omega^2) \left( 1 + \frac{C_c}{C_2} \right) + \frac{1}{C_2} + L_1 \frac{C_c}{C_2}(-\omega^2) + i\omega R_2] \end{aligned} \quad (\text{B.3})$$

Now  $\exp(i\omega t)$  drops out and we can derive the phase difference  $\phi$

$$\exp(i\phi) = \frac{a}{b} \cdot \frac{[L_1(-\omega^2) \left( 1 + \frac{C_c}{C_1} \right) + \frac{1}{C_1} + L_2 \frac{C_c}{C_1}(-\omega^2) + i\omega R_1]}{[L_2(-\omega^2) \left( 1 + \frac{C_c}{C_2} \right) + \frac{1}{C_2} + L_1 \frac{C_c}{C_2}(-\omega^2) + i\omega R_2]} \quad (\text{B.4})$$

For simplicity let's denote

$$\alpha = L_1(-\omega^2) \left( 1 + \frac{C_c}{C_1} \right) + \frac{1}{C_1} + L_2 \frac{C_c}{C_1}(-\omega^2)$$

and

$$\beta = L_2(-\omega^2) \left( 1 + \frac{C_c}{C_2} \right) + \frac{1}{C_2} + L_1 \frac{C_c}{C_2}(-\omega^2)$$

Such that

$$\exp(i\phi) = \frac{a}{b} \cdot \frac{\alpha + i\omega R_1}{\beta + i\omega R_2} = \frac{a}{b} \cdot \frac{\alpha\beta + \omega^2 R_1 R_2 + i\omega(R_1\beta - R_2\alpha)}{\beta^2 + \omega^2 R_2^2}$$

We can then write

$$\exp(i\phi) = \cos(\phi) + i\sin(\phi) = \text{Re} + i\text{Im}$$

It is interesting to look at the case where  $R_1 = R_2 = 0$ . Then

$$\sin(\phi) = 0$$

Telling us that they are always perfectly in or out of phase!  
 When this is not the case we can determine the phase from

$$\tan(\phi) = \frac{\omega(R_1\beta - R_2\alpha)}{\alpha\beta + \omega^2 R_1 R_2} \quad (\text{B.5})$$

if  $R_1 = R_2 = R$ , we can simplify further

$$\tan(\phi) = \frac{\omega R(\beta - \alpha)}{\alpha\beta + \omega^2 R^2} \quad (\text{B.6})$$

And the ratio  $a/b$

$$\frac{a}{b} = \cos(\phi) \frac{\beta^2 + \omega^2 R_2^2}{\alpha\beta + \omega^2 R_1 R_2} \quad (\text{B.7})$$

yields the voltage ratio

$$\frac{V_{C_1}}{V_{C_2}} = \frac{a/C_1}{b/C_2} \quad (\text{B.8})$$



# PCB components

In table C.1 we can see the components used for the resonator PCB. The resonator and matching coil are a part of coil series with the same footprint.

Component	Sub-network	Value	Manufacturer	Manuf. id
Resonator coil	Resonator	100 nH	Coilcraft	1812SMS-R10_L_
Matching capacitor	Matching network	1000 pF	Murata	GRM21A5C2E102JWA1D
Matching Coil	Matching network	10 nH	Coilcraft	1512SP-10N_4E_
Bias tee capacitor	Bias tee	1000 pF	Murata	GRM21A5C2E102JWA1D
Bias tee resistor	Bias tee	100 kOhm	Vishay Dale	TNPW0805100KBEEA
Balun	Input	NA	MiniRF	RFXF2513
RF SMA	Input and Bias tee	NA	Amphenol RF	132291
Trap pins	Output	NA	Mill-Max Manufacturing Corp.	4357-0-00-15-00-00-03-0
Cap div. small cap.	Pick-off	1 pF	Murata Electronics	GQM2195C2E1R0BB12D
Cap div. large cap.	Pick-off	100 pF	Murata Electronics	GQM2195C2E101GB12D

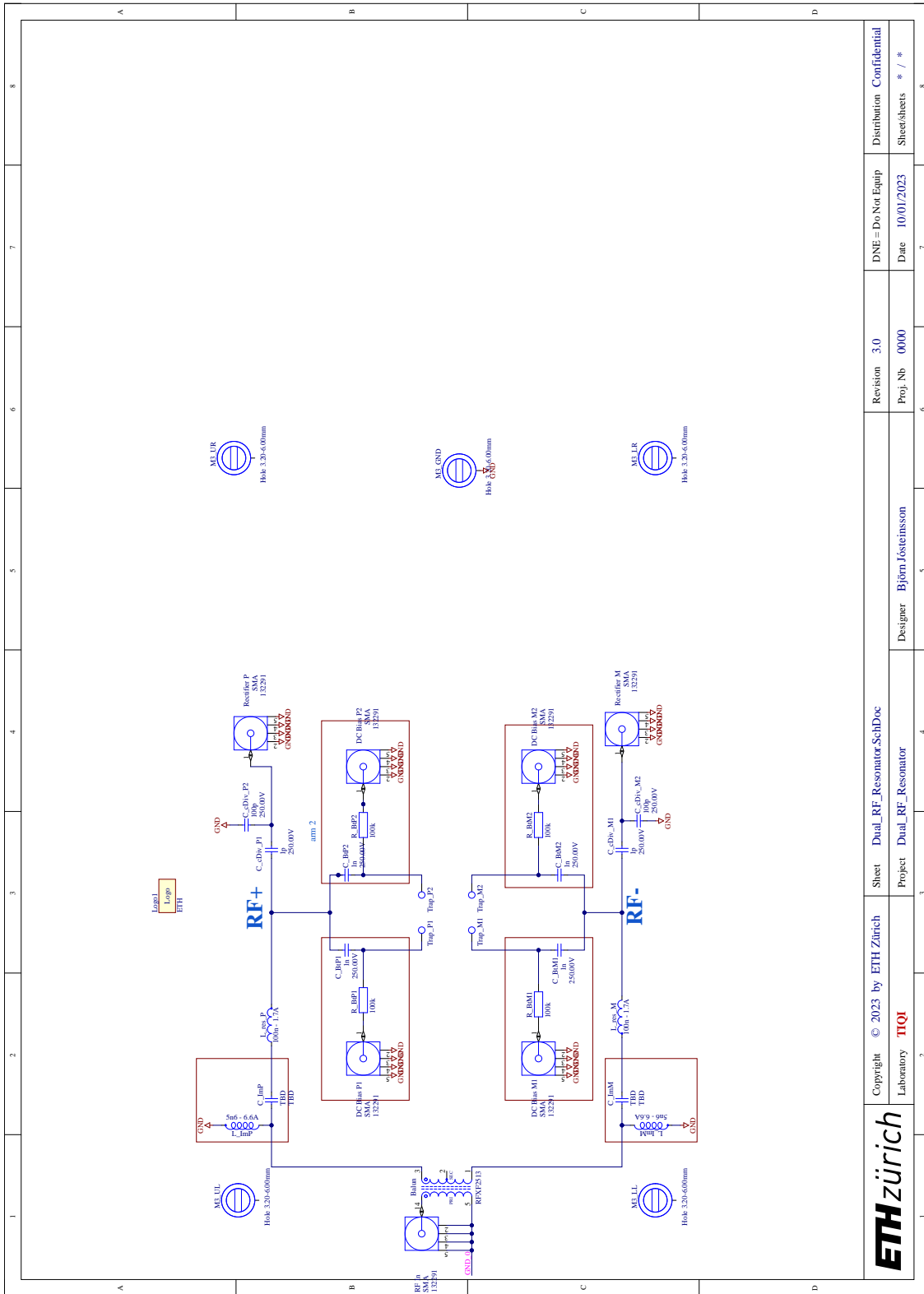
Table C.1.: Components used in the new resonator PCB.

In table C.2 the estimated parasitics from PCB traces, used in LTspice simulations, are seen. The value for these parasitics are calculated by the geometry of the traces (length, width and thickness) and their material properties. Figure C.1 shows the PCB schematic.

C. PCB components

From	To	Length [mm]	L [nH]	C [pF]	R [m $\Omega$ ]
RF in	Balun	6	3.63	0.48	4.86
Balun	$L_{imp}$	9	5.44	0.71	7.29
$L_{imp}$	$C_{imp}$	6.7	4.05	0.53	5.42
$C_{imp}$	$L_{res}$	23.8	14.4	1.88	19.3
$L_{res}$	$C_{div}$	4.2	2.54	0.33	3.4
$C_{div}$	$C_{BT}$	5	3.02	0.40	4.05
$C_{BT}$	$R_{BT}$	3.25	1.97	0.25	2.63
$R_{BT}$	Output pin	14	8.46	1.11	11.3

Table C.2.: PCB trace parasitics calculated from geometry and material properties. The traces have a width of 0.6mm except the one from the RF in to the balun where the width is 1mm.



ETH zürich	Copyright © 2023 by ETH Zürich Laboratory <b>TIQI</b>	Sheet Project	Dual_RF_Resonator Dual_RF_Resonator	Designer Björn Jästelsson	Revision 3.0	DNE = Do Not Equip Date	10/01/2023	Distribution Confidential
					Proj. Nb 0000			Sheet/sheets * / *

Figure C.1.: PCB Schematic.